PLOS ONE

RESEARCH ARTICLE

Flow and hydrodynamic shear stress inside a printing needle during biofabrication

Sebastian J. Müller[1], Elham Mirzahossein[2], Emil N. Iftekhar[2], Christian Bächer[1], Stefan Schrüfer[3,4], Dirk W. Schubert[3,4], Ben Fabry[2], Stephan Gekle[1]*

1 Biofluid Simulation and Modeling, Universität Bayreuth, Bayreuth, Germany, **2** Department of Phyiscs, Friedrich-Alexander Universität Erlangen-Nürnberg, Erlangen, Germany, **3** Institute of Polymer Materials, Friedrich-Alexander Universität Erlangen-Nürnberg, Erlangen, Germany, **4** KeyLab Advanced Fiber Technology, Bavarian Polymer Institute, Fürth, Germany

* stephan.gekle@uni-bayreuth.de

Citation: Müller SJ, Mirzahossein E, Iftekhar EN, Bächer C, Schrüfer S, Schubert DW, et al. (2020) Flow and hydrodynamic shear stress inside a printing needle during biofabrication. PLoS ONE 15(7): e0236371. https://doi.org/10.1371/journal.pone.0236371

Editor: Fang-Bao Tian, University of New South Wales, AUSTRALIA

Received: March 31, 2020

Accepted: July 2, 2020

Published: July 24, 2020

Data Availability Statement: All relevant data are within the manuscript and its Supporting Information files. The Python tool is available at https://github.com/sjmuellerbt/CYprofiles.

Funding: This work was funded by the Deutsche Forschungsgemeinschaft (SFB-TRR 225, project number 326998133, subprojects A01, A07 and B07) (to SJM, EM, SS, DWS, BF and SG). This work was partly funded by the National Institutes of Health grant HL120839 (to BF). Christian Bächer thanks the Studienstiftung des deutschen Volkes

Abstract

We present a simple but accurate algorithm to calculate the flow and shear rate profile of shear thinning fluids, as typically used in biofabrication applications, with an arbitrary viscosity-shear rate relationship in a cylindrical nozzle. By interpolating the viscosity with a set of power-law functions, we obtain a mathematically exact piecewise solution to the incompressible Navier-Stokes equation. The algorithm is validated with known solutions for a simplified Carreau-Yasuda fluid, full numerical simulations for a realistic chitosan hydrogel as well as experimental velocity profiles of alginate and chitosan solutions in a microfluidic channel. We implement the algorithm in an easy-to-use Python tool, included as Supplementary Material, to calculate the velocity and shear rate profile during the printing process, depending on the shear thinning behavior of the bioink and printing parameters such as pressure and nozzle size. We confirm that the shear stress varies in an exactly linear fashion, starting from zero at the nozzle center to the maximum shear stress at the wall, independent of the shear thinning properties of the bioink. Finally, we demonstrate how our method can be inverted to obtain rheological bioink parameters *in-situ* directly before or even during printing from experimentally measured flow rate versus pressure data.

Introduction

Biofabrication, or bioprinting, is a novel technology aimed at applying common 3D printing techniques to fabricate living tissues. In extrusion-based biofabrication, the survival and functionality of printed cells strongly depend on the hydrodynamic stresses that the cells experience during printing [1–5]. These stresses arise mainly from viscous shear forces in the printer nozzle and are thus directly related to the flow profile and the viscosity of the bioink [6–11] in which the cells are suspended. In an effort to reduce hydrodynamics stresses, shear thinning bioinks have been designed that exhibit a nearly flat velocity profile and correspondingly low shear rates in the nozzle center, in contrast to purely Newtonian liquids that develop a parabolic flow profile with higher shear rates throughout most of the nozzle [12–19]. Consequently,

for financial support. Stephan Gekle thanks the Volkswagen Foundation. The funders had no role in study design, data collection and analysis, decision to publish, or preparation of the manuscript.

Competing interests: The authors have declared that no competing interests exist.

cells suspended in shear thinning bioinks can be expected to show increased survival rate and better functionality after printing [4, 16, 20, 21].

To describe the rheology of inelastic, time-independent, shear thinning materials, a variety of viscosity models exists, which are collectively labeled as generalized Newtonian fluids [22]. One of the simplest models assumes a power-law, also known as Ostwald-de Waele relationship [4, 23, 24]. Real shear thinning materials, however, show power-law behavior only in a limited range of shear rates, while Newtonian behavior is observed above and below this range. The latter is particularly relevant for bioprinting applications and prevails in the central region of the printing nozzle where the velocity approaches a constant value and thus a vanishing shear rate. To properly model this behavior, a widely used description is the Carreau-Yasuda (CY) [22, 25] model, which features a central power-law region that smoothly transitions into two Newtonian plateaus in the limits of low and high shear rates. Many commonly used hydrogel materials for bioprinting [26] but also polymer melts or solutions [27] can be accurately characterized with the CY model. Existing methods to calculate theoretically the velocity profile in the printing nozzle for a CY fluid [28, 29] require the shear rate at the nozzle wall as an input parameter. Experimentally, however, this quantity is usually not known. Instead either the pressure difference or the volume flux serve as control parameter.

In this work, we present an algorithm to compute the full velocity, shear rate, and viscosity profile in a printing nozzle for generalized Newtonian fluids such as shear thinning bioinks. Our algorithm is based on interpolating an arbitrary viscosity-shear rate relation by piecewise continuous power-law functions, and requires only the experimentally imposed printing parameters such as the channel radius and the driving pressure difference or flow rate as input values. To allow for an efficient application of our method in everyday laboratory work, we provide a user-friendly implementation of our algorithm for CY fluids as a Python tool included as S1 File. This tool is much simpler to use than typical computational fluid dynamics software and at the same time can provide higher accuracy at much less computational load. The calculated shear stresses are a measure for the mechanical load experienced by cells embedded in the bioink and can thus directly be correlated to post-printing cell viability measurements [1, 11]. We confirm that the well-known linear shear stress distribution found in Newtonian pipe flow is also valid for shear thinning fluids. We validate our algorithm by comparing it to the exact solution for a simplified Carreau-Yasuda fluid, to full numerical Lattice Boltzmann simulations for a realistic chitosan hydrogel under typical printing conditions, and to experimental velocity profiles of a shear thinning alginate solution in a microfluidic channel. Furthermore, we show how our method can be inverted to construct a capillary rheometer, which allows users to determine the rheological parameters of a given bioink using only a bioprinter and a standard laboratory scale without the need of a sophisticated rheometer. Such *in-situ* measurements of bioink rheology combined with the calculation of expected shear rates will help users to optimize the printing process and to achieve the desired printing results especially when bioprinting shear stress-sensitive living cells.

1 Theory and results

1.1 Viscosity model

Our algorithm starts from an experimentally known viscosity-shear rate relation $\eta(\dot{\gamma})$ and interpolates it by a series of power-law functions. The viscosity-shear rate relationship of the bioink, e. g. a cell-laden hydrogel, or any other generalized Newtonian fluid, can be approximated by a continuous, piecewise function as given in (S-1) and depicted in Fig 1a. In every interval, the viscosity-shear rate relation is described by a power-law model $\eta_i(\dot{\gamma}) = K_i\dot{\gamma}^{n_i-1}$

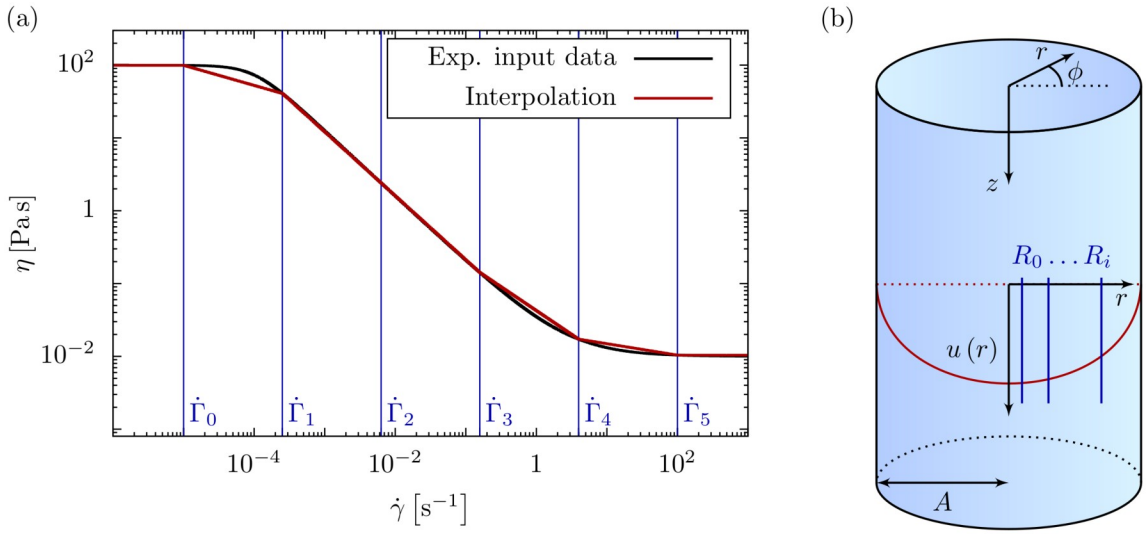

Fig 1. Viscosity and flow profile interpolation. (a) The viscosity-shear rate relationship of an arbitrary shear thinning fluid obtained e. g. from a rheometer measurement is interpolated by power-law intervals. The bounds of the intervals (vertical lines) are given by the intermediate shear rates, $\dot{\Gamma}_i$. By using a large number of intervals, any arbitrary viscosity-shear rate relationship can be approximated as closely as desired. (b) A long cylinder with uniaxial, stationary flow is used as a model for the flow of a bioink through a printer nozzle. The flow profile is split into radial intervals R_i determined implicitly via the intermediate shear rates $\dot{\Gamma}_i$.

https://doi.org/10.1371/journal.pone.0236371.g001

with a consistency parameter K_i and a dimensionless exponent n_i. The i^{th} interval is bounded by the shear rates $\dot{\Gamma}_{i-1}$ and $\dot{\Gamma}_i$, and we demand $\eta(\dot{\gamma})$ to be continuous at these bounds.

This continuity condition together with a set of $\dot{\Gamma}_i$ uniquely determines the power-law parameters K_i and n_i in every interpolation interval, as detailed in section S-1.2.

We note that this approach can be applied to any material described in terms of generalized Newtonian fluids, including yield stress fluids. Furthermore, our method includes cell-laden bioinks, as, on the one hand, the presence of cells has been shown to only slightly alter the materials' rheological behavior [5, 30]. On the other hand, the macroscopic rheology of a cell suspension, determined e. g. via shear rheometry or our capillary rheometry method presented in section 3, can be used as input for our method.

1.2 Governing equations

Analogously to the well-known Poiseuille flow of a Newtonian fluid [31, pp. 180 ff.], we assume a stationary, laminar, and pressure driven flow, with the velocity having only an axial component u depending on the radial position r. We consider a cylindrical channel and neglect entrance and exit effects. Applying these flow conditions, the incompressible Navier-Stokes equations reduce to the ordinary differential equation as shown in section S-1.3:

$$G = \frac{1}{r}\frac{\partial}{\partial r}\left(r\eta(\dot{\gamma})\frac{\partial u}{\partial r}\right) \tag{1}$$

Here, the constant pressure gradient $G := \frac{\partial p}{\partial z} = \frac{\Delta p}{L}$ is defined by the pressure drop $\Delta p = p_0 - p_L < 0$ over a channel segment of length L. For a Newtonian fluid, i. e. $\eta(\dot{\gamma}) = \eta$, integration of Eq (1) directly yields the well-known linear radial dependency of the shear stress:

$$\sigma(r) = \eta\dot{\gamma} = -\frac{G}{2}r \tag{2}$$

Similar to the piecewise viscosity model in Fig 1a, we decompose the axial velocity $u(r)$ and the shear rate $\dot{\gamma}(r)$ into radial intervals R_i as given in (S-29) and (S-32) and illustrated in Fig 1b for the velocity.

Inserting these piecewise profiles into the Navier-Stokes equation Eq (1) yields the following system of equations where i denotes the intervals as above:

$$G = \frac{1}{r}\frac{\partial}{\partial r}[-rK_i(\dot{\gamma}_i(r))^{n_i}] \tag{3}$$

$$\dot{\gamma}_i(r) = -\frac{\partial u_i(r)}{\partial r} \tag{4}$$

In order to solve this system of equations we assume the axial velocity to be continuously differentiable and the shear rate to be continuous. The flow shall further fulfill a no-slip boundary condition at the channel wall and have its maximum at the channel center. The mathematical solution to the system of equations Eqs (3) and (4) is detailed in section S-1.4 and section S-1.5 and can be summarized as follows: the shear rate profile is obtained by integrating Eq (3) over the radial position once. Inserting this solution into Eq (4) yields the velocity profile after another integration over r. Both integrations come along with integration constants that are determined employing the boundary conditions of the flow and the continuity conditions as stated above.

1.3 Results

The first equation Eq (3) can be rearranged and integrated once to obtain the shear rate profile in the i^{th} interval:

$$\dot{\gamma}_i(r) = \left(-\frac{G}{2K_i}r\right)^{\frac{1}{n_i}} \tag{5}$$

From this, the velocity profile is obtained by integrating over r, which ultimately yields (cf. (S-58)):

$$\begin{aligned} u_i(r) = & -\left(-\frac{G}{2K_i}\right)^{\frac{1}{n_i}}\frac{n_i}{n_i+1}r^{1+\frac{1}{n_i}} \\ & +\left(-\frac{G}{2K_k}\right)^{\frac{1}{n_k}}\frac{n_k}{n_k+1}A^{1+\frac{1}{n_k}} \\ & -\sum_{j=i}^{k-1}R_j\dot{\Gamma}_j\left(\frac{n_{j+1}}{n_{j+1}+1}-\frac{n_j}{n_j+1}\right) \end{aligned} \tag{6}$$

Here, the newly introduced index k denotes the radial interval that contains the physical boundary of the channel, i. e. $R_{k-1} \leq A \leq R_k$ with the channel radius A.

The radial shear stress profile can, similarly to the Newtonian case, be derived from Eq (1), yielding the same linear behavior:

$$\sigma(r) = -\eta(\dot{\gamma})\frac{\partial u}{\partial r} = -\frac{G}{2}r \tag{7}$$

This shows that the shear stress profile in a cylindrical channel is independent of the shear thinning properties of the material.

Using the solutions for the shear rate (5) and the velocity (6), we derive mathematical expressions for the flow rate as well as the average velocity, shear rate, viscosity, and shear

stress. Details of the derivation and the corresponding solutions can be found in (S-63), (S-66), (S-71) and (S-74), respectively (cf. section S-1.6). The flow rate or, equivalently, the average flow velocity determines the printing speed in 3D bioprinting processes. The average shear rate and shear stress can be used to estimate cell damage during printing [2, 4] as detailed in section S-1.8 of the S1 File. We discuss the inclusion of possible wall-slip effects [35] in section S-1.9 of the S1 File.

2 Validation

To validate our method, we implement the presented algorithm in a Python [32] tool, included as S1 File together with an explanatory tutorial in section S-3 and available at https://github.com/sjmuellerbt/CYprofiles. Our tool performs the viscosity interpolation according to section 1.1 for a five-parameter Carreau-Yasuda fluid, given in Eq (9). The radial profiles for velocity, shear rate, viscosity, and shear stress and their respective averaged quantities are calculated after providing the printing parameters, i. e. the nozzle radius and the pressure gradient or an imposed flow rate.

We first validate our algorithm using an exact global mathematical solution for a simplified CY model. Next, we compare our algorithm with Lattice Boltzmann simulations for a general CY model using the open source software package ESPResSo [33, 34], for which we extended both the CPU and GPU implementation with several inelastic viscosity models, including the CY model. We finally perform experimental velocity profile measurements in a microfluidic channel and confirm the theoretical prediction of our Lattice Boltzmann simulations.

2.1 Validation with global solution

We consider a simplified Carreau-Yassuda (CY) model of the following form

$$\tilde{\eta}(\dot{\gamma}) = \frac{\tilde{\eta}_0}{1 + K\dot{\gamma}} \tag{8}$$

where $\tilde{\eta}_0$ is the viscosity in the limit of zero shear rate and K is a time constant. For this model, an exact global solution to the NSE Eq (1) can be found as described in(S-79) and (S-81) (cf. section S-1.7). As shown in Fig 2, we find excellent agreement between this exact solution and the calculated profiles using our Python tool.

2.2 Validation with Lattice Boltzmann simulations

The general CY model [25] is given by

$$\tilde{\eta}(\dot{\gamma}) = \tilde{\eta}_\infty + \frac{\tilde{\eta}_0 - \tilde{\eta}_\infty}{[1 + (K\dot{\gamma})^{a_1}]^{\frac{a_2}{a_1}}}, \tag{9}$$

where $\tilde{\eta}_\infty$ is the viscosity in the limit of infinite shear rates and the exponents a_1 and a_2 determine the shape of the transition between the zero-shear Newtonian plateau and the power-law region as well as the power-law behavior. For this general CY fluid a global mathematical solution to the NSE does not exist. We therefore compare our algorithm to Lattice-Boltzmann simulations using realistic bioink and printing parameters for a chitosan hydrogel taken from [26] with the following rheological parameters: $\tilde{\eta}_0 = 5807$ Pas, $K = 5.33$ s, $a_1 = 1.35$ and $a_2 = 0.87$. The simulation setup consists of a $5 \times 400 \times 400$ ($x \times y \times z$) box with a cylindrical boundary along the x-axis corresponding to a physical radius of $A = 100$ μm. The flow is periodic in x-direction thus leading to an effectively infinitely long channel. Further details of the Lattice-Boltzmann simulations are given in the S1 File.

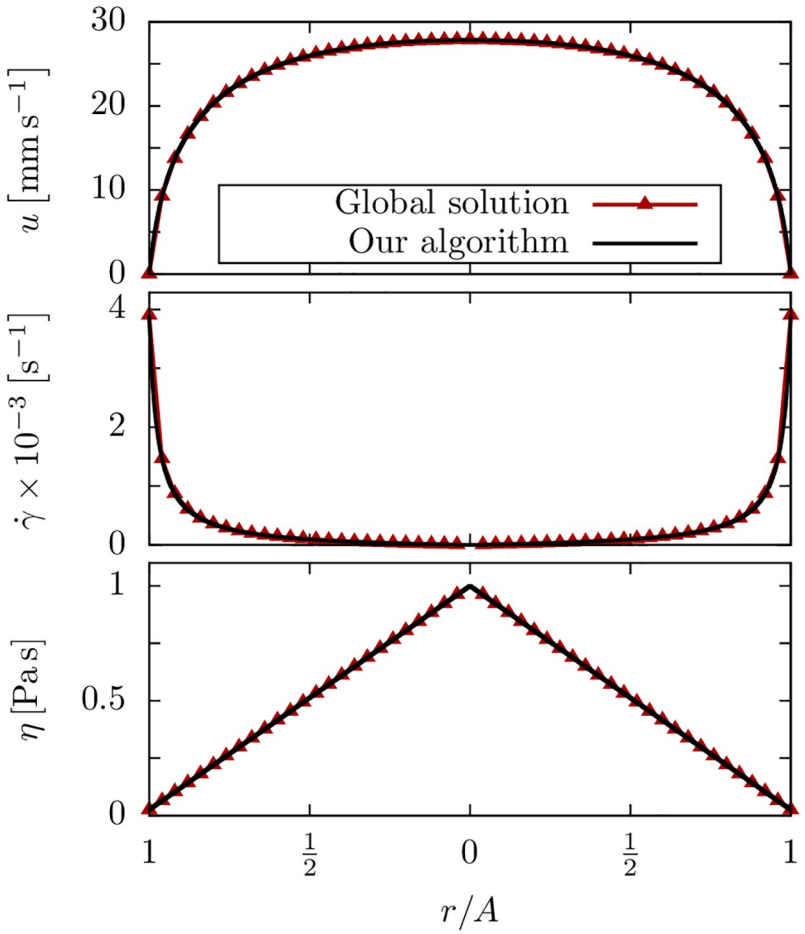

Fig 2. Validation with a mathematical solution. Flow profiles for the simplified CY model: the global mathematical solution and the prediction by our algorithm agree very well. The parameters are $N = 1000$, $\eta_0 = 100$ Pa s, $K = 1.0$ s and $G = -1.95 \times 10^6$ Pa m^{-1}.

https://doi.org/10.1371/journal.pone.0236371.g002

The calculated and simulated flow profiles are in excellent agreement (Fig 3) thus validating our algorithm for a general CY fluid.

2.3 Validation with experimental flow profile measurements

As experimental proof, we measure the flow profile of an alginate solution along the centerline of a microchannel and compare our findings to Lattice Boltzmann simulations of the same geometry.

We prepare a 2.0% alginate solution by mixing 800 mg of alginate (Grindsted PH 176, Dupont, USA) in 50 ml Dulbecco's phosphate buffered saline under constant stirring overnight at room temperature together with yellow-green fluorescent beads (FluoroSphere carboxylated beads, Invitrogen, diameter: 0.5 μm). The alginate solution is injected under defined pressure into a polymethylmetacrylate microfluidic channel equipped with male mini Luer lock connectors (Darwin Microfluidics, France, internal volume: 8 μl) via a 15 cm long silicon tube (inner diameter: 1 mm). The channel has a length of 58 mm and a quadratic cross section of 190 μm × 190 μm, similar in size to the cross section of a typical printing needle. A square cross section of the channel was chosen to avoid optical distortions that would arise from the

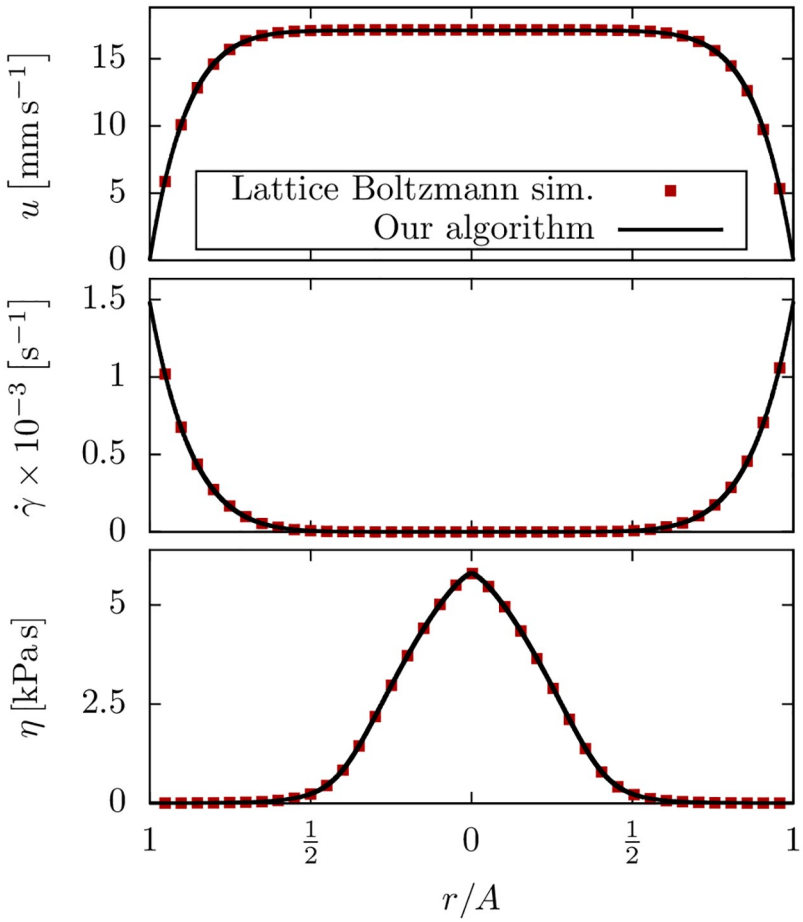

Fig 3. Validation with Lattice Boltzmann calculations. Flow profiles of a chitosan hydrogel with a pressure gradient of $G = -7.0 \times 10^7$ Pa m^{-1} and $N = 1000$.

https://doi.org/10.1371/journal.pone.0236371.g003

curvature of a cylindrical glass capillary in combination with the refractive index differences between glass and alginate. We visualize the flow of alginate using an epifluorescence microscope (DM4, Leica Microsystems, Germany) equipped with a CCD camera (frame rate: 100 Hz, Prosilica GE680, Allied Vision, Germany) and a 100 mW laser diode (473 nm). The microscope is focussed at the mid-section of the channel (height: 95 μm).

We perform measurements at a pressure of 300 kPa, close to actual printing conditions. The maximum flow speed in the center of the channel is around 2 cm s^{-1}, which is too fast to track the beads between successive frames. Instead, the velocity is estimated from the length of the linear streaks of the beads during exposure, as shown in Fig 4a, divided by the exposure time of 7 ms.

We perform Lattice Boltzmann simulations of the pressure driven flow of the alginate solution in a square microchannel. The simulation setup consists of a $5 \times 400 \times 400$ ($x \times y \times z$) box with plane boundaries in y- and z-direction forming a square channel that corresponds to the 190 μm × 190 μm microfluidic channel used in the experiment. The viscosity parameters were obtained using our capillary rheometry method described in section 3 as $\tilde{\eta}_0 = 3.65$ Pas, $\dot{\gamma}_c = 21.71$ s^{-1} and $\alpha = 0.67$, according to equation Eq (10) below. Since we do not know the pressure drop across the mini Luer-lock connectors and tubings, we estimate the pressure gradient from the maximum flow speed measured at the center of the channel. Accordingly, we

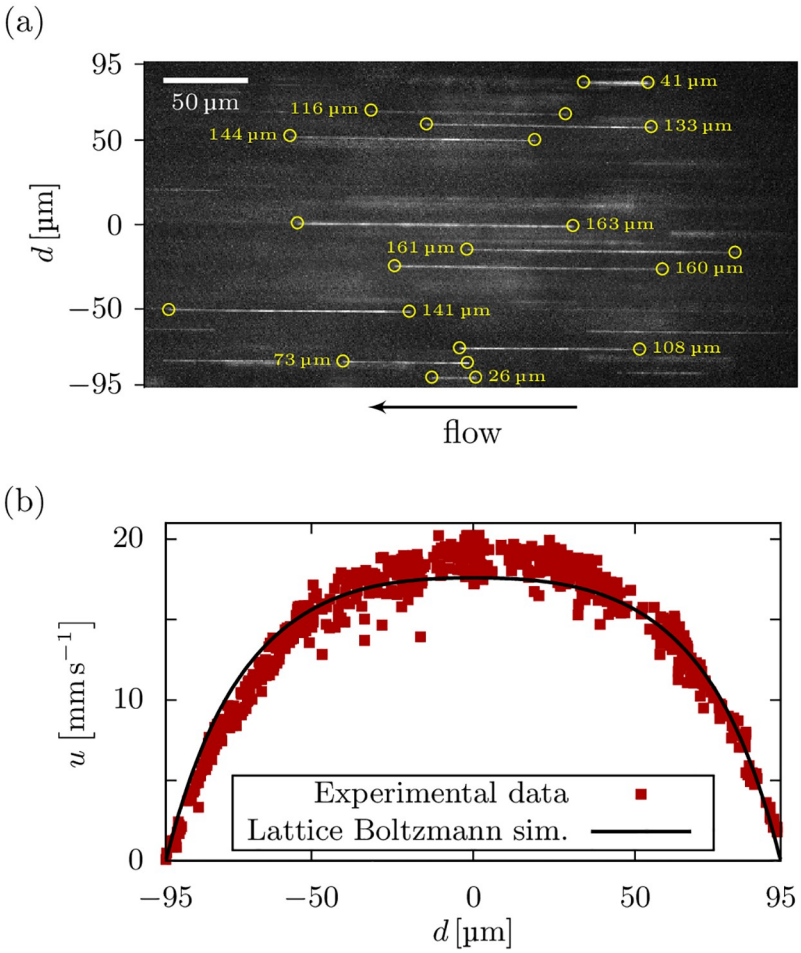

Fig 4. Validation with experimental flow measurements. Experimental measurement of the flow profile of a 2% alginate solution in a 190 µm × 190 µm microchannel. (a) Example micrograph of the bead tracking procedure. The velocity with respect to the lateral position is obtained as the length (yellow circles and labels) of the streaks divided by the exposure time. (b) The measured flow profile is in excellent agreement with our Lattice Boltzmann simulations.

https://doi.org/10.1371/journal.pone.0236371.g004

find that 79% of the total pressure drop of 300 kPa occurs across the 58 mm long channel, while the mini Luer-lock connectors and tubings account for the remaining 21%.

Fig 4b depicts the measured flow profile in comparison to our Lattice Boltzmann simulations. We see excellent agreement of the measured velocity profile and our numerical prediction. Further measurements of alginate hydrogels with different concentrations, as well as a chitosan hydrogel, at various printing pressures and in different channel geometries are included as S1 File.

3 Inverse application for a capillary rheometer

Not all laboratories working in bioprinting may have access to sophisticated rheometers for measuring the non-linear viscosity of their bioinks. Moreover, bioinks are often highly sensitive fluids with a large batch-to-batch variation, and the sample used for rheometer measurements may not behave in the same way as the sample used for the actual printing process. In this section, we show how our method can be inverted to perform *in-situ* capillary rheometry measurements using only a bioprinter and a standard laboratory scale. For this, we measure

the pressure versus flow rate relationship [35] for a range of discrete pressure values. Using our Python tool, we then extract from this data the non-linear viscosity parameters of the bioink.

3.1 Experimental setup

We prepare a 2.5% alginate solution using the protocol described in section 2.3 without the addition of fluorescent beads. We measure the viscosity of the alginate solution at a temperature of 25˚C at shear rates between 0.01 s^{-1} and 100 s^{-1} using a cone-plate rheometer (DHR-3, TA-Instruments, USA). Alternatively, we measure the viscosity with a custom-made bioprinter that we use here as a capillary rheometer. A schematic of the experimental setup is shown in Fig 5. The alginate solution is driven with a defined pressure (K8P electronic pressure regulator, Camozzi Automation, Italy) through a steel needle (21G blunt cannula #9180109-02, B-Braun, Germany, 28 mm length, 551 μm inner diameter). The pressure is increased stepwise from 20 kPa to 200 kPa in steps of 20 kPa. The driving pressure is measured with a pressure

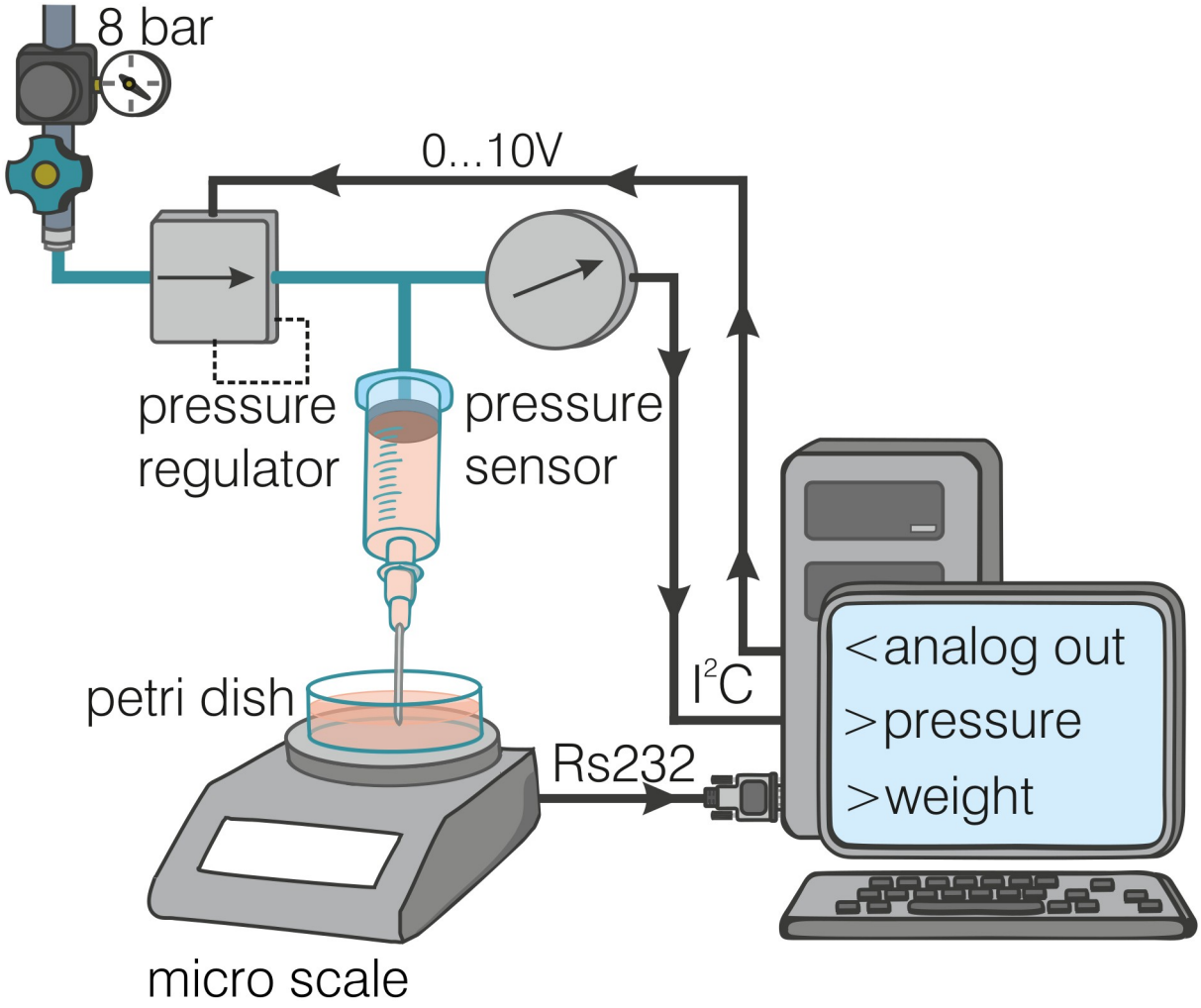

Fig 5. Experimental capillary rheometer setup. Schematic of the experimental setup using a custom-made bioprinter as capillary rheometer: the bioink is driven through a syringe under defined pressure, and the flow rate of the extruded alginate is measured with a precision scale.

https://doi.org/10.1371/journal.pone.0236371.g005

transducer (DRMOD-I2C-R10B, B+B Thermo-Technik GmbH, Germany), and the flow rate of the extruded alginate is measured with a precision scale (DI-100, Denver Instrument, USA).

We then fit the zero-shear viscosity, $\tilde{\eta}_0$, the corner shear rate, $\dot{\gamma}_c$, and the power-law shear thinning exponent, α, of a 3-parameter Carreau-Yasuda fluid to match the measured flow rate versus pressure relationship. The viscosity-shear rate relationship is given by

$$\tilde{\eta}(\dot{\gamma}) = \tilde{\eta}_0 \left[1 + \left(\frac{\dot{\gamma}}{\dot{\gamma}_c}\right)^{\alpha}\right]^{-1} \quad , \tag{10}$$

which is derived from Eq (9) by omitting the infinite-shear viscosity ($\tilde{\eta}_\infty = 0$), and introducing the corner-shear rate $\dot{\gamma}_c = K^{-1}$ as well as the single exponent $\alpha = a_1 = a_2$. Fitting is performed using a Marquard-Levenberg least-squares method implemented in the Python library SciPy, where the squared difference between the measured and the computed flow rate is minimized for each pressure level. The flow rate is computed according to (S-64) with the printing parameters mentioned above and $N = 150$ interpolation intervals between shear rates of 10^{-6} s^{-1} to 10^8 s^{-1}. Since the inner diameter of the printer cartridge is large compared to that of the nozzle, we neglect a possible pressure drop along the cartridge.

3.2 Results

When measured with a cone-plate rheometer, the viscosity of a 2.5% alginate solution displays a pronounced shear rate dependency (Fig 6a), which is well described by a 3-parameter CY model according to Eq (10). Specifically, at shear rates below the corner shear rate $\dot{\gamma}_c \approx 17.8\ s^{-1}$, the viscosity is approximately constant, with $\tilde{\eta}_0 \approx 7.9$ Pas. At shear rates above $\dot{\gamma}_c$, the viscosity decreases according to a power-law with exponent $\alpha \approx 0.74$.

When the same 2.5% alginate solution is extruded through a 28 mm long 551 μm diameter capillary, we find an over-proportional increase in flow rate with increasing pressure (Fig 6b). Specifically, a doubling in pressure causes an approximately 10-fold increase in flow rate. This experimentally measured flow rate versus pressure relationship is exactly predicted by our numerical solution (blue line in Fig 6b), adding further support to the validity of our algorithm.

If a rheometer is not available, the above procedure can be inverted to obtain the rheological properties of the bioink as follows: starting from a first guess of the CY parameters, the pressure versus flow rate is computed using our Python tool. Subsequently, the viscosity parameters are refined until the prediction matches with the experimental data as shown in Fig 6b. The parameters obtained from the flow-rate versus pressure data (red squares in Fig 6b) are $\tilde{\eta}_0 \approx 6.8$ Pas, $\dot{\gamma}_c \approx 27.9\ s^{-1}$, and $\alpha \approx 0.78$ and differ only slightly from the parameters extracted from the cone-plate rheometer measurements. Accordingly, also only a slight difference between both parameter sets is seen in the velocity, shear rate and viscosity profiles shown in Fig 7. Also visible in Fig 6b is an increasing deviation of the flow rate versus pressure prediction for the cone-plate rheometer from the measured data with increasing pressure. This is likely due to shear rheometers not being able to achieve the large shear rates that occur under realistic printing conditions, while the capillary rheometer method intrinsically accounts for that.

A specific advantage of this capillary rheometry approach is that the experiment can be performed with the very same bioink that is currently in the printing cartridge prior to the actual printing process. Since most bioprinters are pressure controlled, i.e. the bioink is extruded through a printing needle with a constant pressure, the highly non-linear increase of the flow rate with increasing pressure makes it difficult to find the optimal printing parameters and to

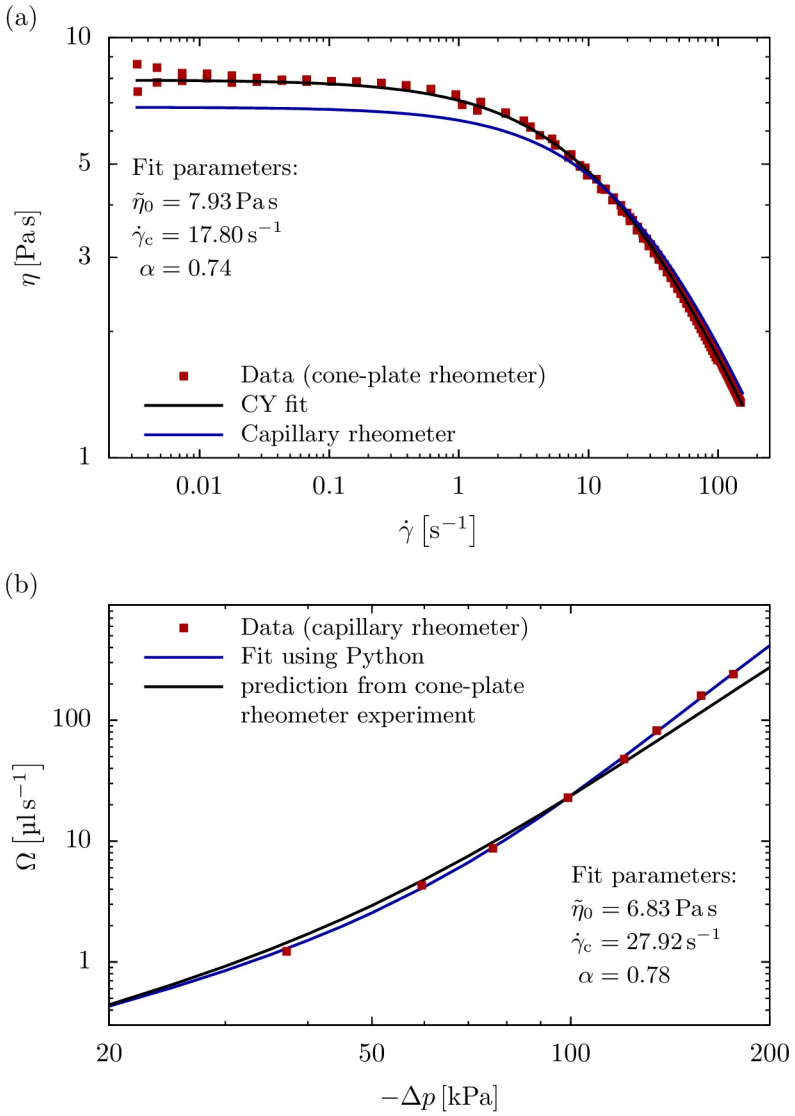

Fig 6. Comparison between capillary rheometer and cone-plate rheometer results. (a) Viscosity versus shear rate for a 2.5% alginate solution as measured with a cone-plate rheometer (data from 4 independent measurements, red squares) shows the pronounced shear thinning of a CY fluid that is well characterized by 3 fit parameters (black line) according to Eq (10). This shear thinning behavior can be predicted (blue line) from an independent capillary rheometry experiment using our Python tool. (b) Flow rate versus pressure relationship of the alginate solution when extruded through a 28 mm long 551 μm diameter capillary (red squares). This relationship follows our numerical solution using 3 fit parameters (blue line). The flow rate versus pressure relationship can similarly be predicted (black line) from the viscosity values obtained from an independent cone-plate rheometer experiment shown in the upper panel, showing significant deviations with increasing pressure.

https://doi.org/10.1371/journal.pone.0236371.g006

predict the material shear stresses during the printing process. Our algorithm solves both problems.

Conclusion

We presented a simple yet highly accurate algorithm to calculate the velocity and shear rate profiles for generalized Newtonian fluids, such as shear thinning bioinks, in cylindrical nozzles. For this, an arbitrary experimentally known viscosity-shear rate relation is split into a set

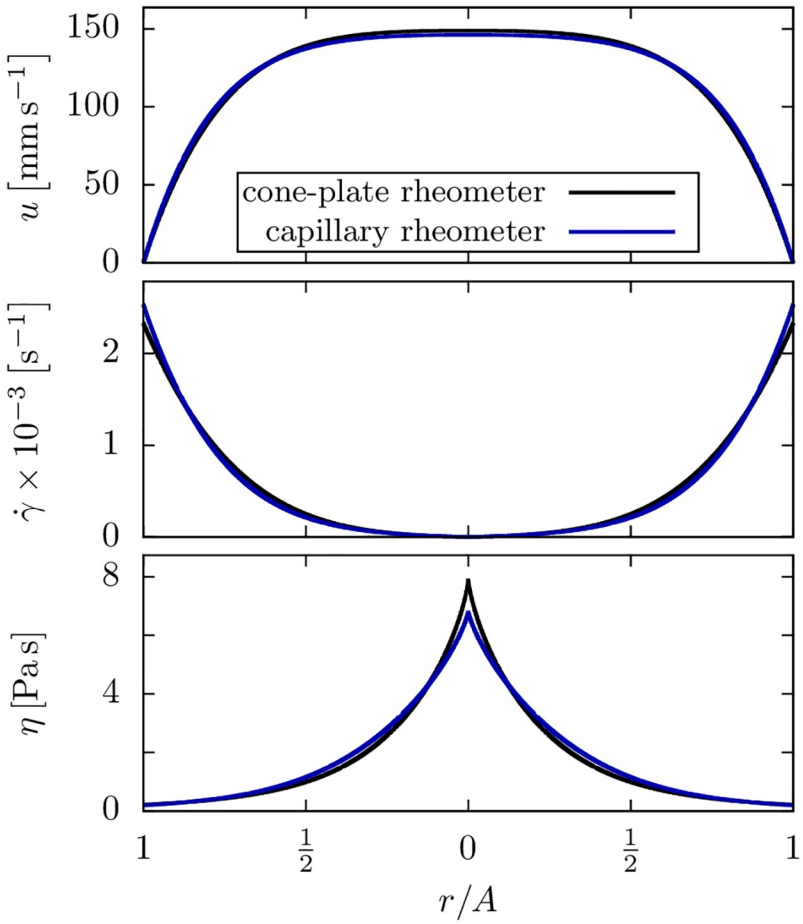

Fig 7. Alginate flow profile from capillary rheometer and cone-plate rheometer data. Flow profiles of 2.5% alginate hydrogel with a pressure difference of $\Delta p = -10^5$ Pa and $N = 150$. There is only a slight difference between the flow profiles calculated from the viscosity parameters obtained with a cone-plate rheometer (black line) and our capillary rheometer (blue line).

https://doi.org/10.1371/journal.pone.0236371.g007

of continuous intervals described by power-laws. This includes the possibility to predict velocity and shear stress profiles in pure as well as cell-laden bioinks. In each interval, an exact solution for the shear rate and velocity is computed and connected to neighboring intervals to obtain a continuous smooth profile over the entire nozzle diameter. For the shear stress, the linear radial dependency independent of the fluid rheology was confirmed. In addition, the total flow rate as well as the average viscosity, shear rate and shear stress are also found mathematically.

We implemented our method as an easy-to-use Python tool for calculating the velocity and shear rate profiles for a Carreau-Yasuda fluid. To validate this tool, we compared our predictions to a mathematically exact global solution and to Lattice Boltzmann simulations for realistic chitosan hydrogels under typical bioprinting conditions. In both cases, we found excellent agreement. We further measured the velocity profile of an alginate solution in a microfluidic channel and found good agreement with Lattice Boltzmann simulations.

An important experimental application of our theoretical method is capillary rheometry. Here, the flow rate versus pressure relationship for a given hydrogel is obtained using a standard bioprinter. This data can then be fit to our theoretical predictions yielding the

corresponding rheological parameters of the bioink. We illustrated this application for alginate and found good agreement with classical rheometer data.

Our method and the accompanying Python implementation provide a fast and simple tool to predict flow rates and shear stresses during bioprinting for a given bioink and thus will help to optimize printing parameters, especially for shear stress-sensitive living cells.

Supporting information

S1 File. Mathematical derivation, further experimental validation, and user's guide. The supplementary material for the manuscript contains a detailed mathematical derivation of the presented method and a simple model to estimate the force and deformation experienced by a cell in shear thinning capillary flow. We also include further experimental measurements for alginate 2% and 3% and chitosan 3% in square and rectangular microchannels, as well as the corresponding error calculations. A user's guide for the developed Python tool is provided.
(PDF)

S2 File. CYprofiles.py. File containing the implemented classes of our tool.
(PY)

S3 File. Tutorial.py. File with a basic usage example for the implemented classes.
(PY)

Acknowledgments

We thank Werner Schneider and Jia You for designing and building the capillary rheometer and for performing the measurements, Lena Fischer and Rainer Detsch for help with alginate preparation, Delf Kah, Alexander Winterl and Christoph Mark for help with the development of the bioprinter control software, and Ronny Reimann for the creating the experimental setup schematic. We gratefully acknowledge computing time provided by the SuperMUC system of the Leibniz Rechenzentrum, Garching, as well as by the Bavarian Polymer Institute (BPI). Christian Bächer acknowledges support by the study program "Biological Physics" of the Elite Network of Bavaria.

Author Contributions

Formal analysis: Sebastian J. Müller, Christian Bächer.

Funding acquisition: Dirk W. Schubert, Ben Fabry, Stephan Gekle.

Investigation: Elham Mirzahossein, Emil N. Iftekhar, Stefan Schrüfer.

Methodology: Sebastian J. Müller, Elham Mirzahossein, Emil N. Iftekhar.

Software: Sebastian J. Müller.

Supervision: Dirk W. Schubert, Ben Fabry, Stephan Gekle.

Writing – original draft: Sebastian J. Müller, Stephan Gekle.

Writing – review & editing: Sebastian J. Müller, Ben Fabry, Stephan Gekle.

References

1. Blaeser A, Duarte Campos DF, Puster U, Richtering W, Stevens MM, Fischer H. Controlling Shear Stress in 3D Bioprinting is a Key Factor to Balance Printing Resolution and Stem Cell Integrity. Advanced Healthcare Materials. 2015; 5(3):326–333. https://doi.org/10.1002/adhm.201500677 PMID: 26626828

2. Snyder J, Rin Son A, Hamid Q, Wang C, Lui Y, Sun W. Mesenchymal stem cell printing and process regulated cell properties. Biofabrication. 2015; 7(4):044106–17. https://doi.org/10.1088/1758-5090/7/4/044106 PMID: 26696405
3. Zhao Y, Li Y, Mao S, Sun W, Yao R. The influence of printing parameters on cell survival rate and printability in microextrusion-based 3D cell printing technology. Biofabrication. 2015; 7(4):045002–11. https://doi.org/10.1088/1758-5090/7/4/045002 PMID: 26523399
4. Paxton N, Smolan W, Böck T, Melchels F, Groll J, Jüngst T. Proposal to assess printability of bioinks for extrusion-based bioprinting and evaluation of rheological properties governing bioprintability. Biofabrication. 2017; 9(4):044107. https://doi.org/10.1088/1758-5090/aa8dd8 PMID: 28930091
5. Emmermacher J, Spura D, Cziommer J, Kilian D, Wollborn T, Fritsching U, et al. Engineering Considerations on Extrusion-Based Bioprinting: Interactions of Material Behavior, Mechanical Forces and Cells in the Printing Needle. Biofabrication. 2020; 12(2):025022. https://doi.org/10.1088/1758-5090/ab7553 PMID: 32050179
6. Malda J, Visser J, Melchels FP, Jüngst T, Hennink WE, Dhert WJA, et al. 25th Anniversary Article: Engineering Hydrogels for Biofabrication. Advanced Materials. 2013; 25(36):5011–5028. https://doi.org/10.1002/adma.201302042 PMID: 24038336
7. Zuidema JM, Rivet CJ, Gilbert RJ, Morrison FA. A protocol for rheological characterization of hydrogels for tissue engineering strategies. Journal of Biomedical Materials Research Part B: Applied Biomaterials. 2013; 102(5):1063–1073. https://doi.org/10.1002/jbm.b.33088
8. Tian XY, Li MG, Cao N, Li JW, Chen XB. Characterization of the flow behavior of alginate/hydroxyapatite mixtures for tissue scaffold fabrication. Biofabrication. 2009; 1(4):045005. https://doi.org/10.1088/1758-5082/1/4/045005 PMID: 20811114
9. Sarker B, Rompf J, Silva R, Lang N, Detsch R, Kaschta J, et al. Alginate-based hydrogels with improved adhesive properties for cell encapsulation. International Journal of Biological Macromolecules. 2015; 78:72–78. https://doi.org/10.1016/j.ijbiomac.2015.03.061 PMID: 25847839
10. Leppiniemi J, Lahtinen P, Paajanen A, Mahlberg R, Metsä-Kortelainen S, Pinomaa T, et al. 3D-Printable Bioactivated Nanocellulose–Alginate Hydrogels. ACS Applied Materials & Interfaces. 2017; 9(26):21959–21970. https://doi.org/10.1021/acsami.7b02756
11. Shi J, Wu B, Li S, Song J, Song B, Lu WF. Shear stress analysis and its effects on cell viability and cell proliferation in drop-on-demand bioprinting. Biomedical Physics & Engineering Express. 2018; 4(4):045028. https://doi.org/10.1088/2057-1976/aac946
12. Nair K, Gandhi M, Khalil S, Yan KC, Marcolongo M, Barbee K, et al. Characterization of cell viability during bioprinting processes. Biotechnology Journal. 2009; 4(8):1168–1177. https://doi.org/10.1002/biot.200900004 PMID: 19507149
13. Highley CB, Rodell CB, Burdick JA. Direct 3D Printing of Shear-Thinning Hydrogels into Self-Healing Hydrogels. Adv Mater. 2015; 27(34):5075–5079. https://doi.org/10.1002/adma.201501234 PMID: 26177925
14. Larsen BE, Bjørnstad J, Pettersen EO, Tønnesen HH, Melvik JE. Rheological characterization of an injectable alginate gel system. BMC Biotechnol. 2015; 15(1). https://doi.org/10.1186/s12896-015-0147-7
15. Hölzl K, Lin S, Tytgat L, Van Vlierberghe S, Gu L, Ovsianikov A. Bioink properties before, during and after 3D bioprinting. Biofabrication. 2016; 8(3):032002. https://doi.org/10.1088/1758-5090/8/3/032002 PMID: 27658612
16. Ouyang L, Yao R, Zhao Y, Sun W. Effect of bioink properties on printability and cell viability for 3D bioplotting of embryonic stem cells. Biofabrication. 2016; 8(3):035020–12. https://doi.org/10.1088/1758-5090/8/3/035020 PMID: 27634915
17. Jüngst T, Smolan W, Schacht K, Scheibel T, Groll J. Strategies and Molecular Design Criteria for 3D Printable Hydrogels. Chem Rev. 2016; 116(3):1496–1539. https://doi.org/10.1021/acs.chemrev.5b00303 PMID: 26492834
18. Jose RR, Rodriguez MJ, Dixon TA, Omenetto F, Kaplan DL. Evolution of Bioinks and Additive Manufacturing Technologies for 3D Bioprinting. ACS Biomater Sci Eng. 2016; 2(10):1662–1678. https://doi.org/10.1021/acsbiomaterials.6b00088
19. Thakur A, Jaiswal MK, Peak CW, Carrow JK, Gentry J, Dolatshahi-Pirouz A, et al. Injectable shear-thinning nanoengineered hydrogels for stem cell delivery. Nanoscale. 2016; 8(24):12362–12372. https://doi.org/10.1039/C6NR02299E PMID: 27270567
20. Markstedt K, Mantas A, Tournier I, Martínez Ávila H, Hägg D, Gatenholm P. 3D Bioprinting Human Chondrocytes with Nanocellulose–Alginate Bioink for Cartilage Tissue Engineering Applications. Biomacromolecules. 2015; 16(5):1489–1496. https://doi.org/10.1021/acs.biomac.5b00188 PMID: 25806996

21. Ning L, Betancourt N, Schreyer DJ, Chen X. Characterization of Cell Damage and Proliferative Ability during and after Bioprinting. ACS Biomaterials Science & Engineering. 2018; 4(11):3906–3918. https://doi.org/10.1021/acsbiomaterials.8b00714

22. Phillips TN, Roberts GW. Lattice Boltzmann models for non-Newtonian flows. IMA Journal of Applied Mathematics. 2011; 76(5):790–816. https://doi.org/10.1093/imamat/hxr003

23. Ostwald W. Ueber die rechnerische Darstellung des Strukturgebietes der Viskosität. Kolloid-Zeitschrift. 1929; 47(2):176–187. https://doi.org/10.1007/BF01496959

24. Blair GWS, Hening JC, Wagstaff A. The Flow of Cream through Narrow Glass Tubes. The Journal of Physical Chemistry. 1939; 43(7):853–864. https://doi.org/10.1021/j150394a004

25. Carreau PJ. Rheological Equations from Molecular Network Theories. Transactions of the Society of Rheology. 1972; 16(1):99–127. https://doi.org/10.1122/1.549276

26. Wu Q, Therriault D, Heuzey MC. Processing and Properties of Chitosan Inks for 3D Printing of Hydrogel Microstructures. ACS Biomaterials Science & Engineering. 2018; 4(7):2643–2652. https://doi.org/10.1021/acsbiomaterials.8b00415

27. Escudier MP, Gouldson IW, Pereira AS, Pinho FT, Poole RJ. On the reproducibility of the rheology of shear-thinning liquids. Journal of Non-Newtonian Fluid Mechanics. 2001; 97(2-3):99–124. https://doi.org/10.1016/S0377-0257(00)00178-6

28. Cruz DA, Coelho PM, Alves MA. A Simplified Method for Calculating Heat Transfer Coefficients and Friction Factors in Laminar Pipe Flow of Non-Newtonian Fluids. Journal of Heat Transfer. 2012; 134 (9):091703. https://doi.org/10.1115/1.4006288

29. Sochi T. Analytical solutions for the flow of Carreau and Cross fluids in circular pipes and thin slits. Rheologica Acta. 2015; 54(8):745–756. https://doi.org/10.1007/s00397-015-0863-x

30. Manojlovic V, Djonlagic J, Obradovic B, Nedovic V, Bugarski B. Investigations of Cell Immobilization in Alginate: Rheological and Electrostatic Extrusion Studies. Journal of Chemical Technology & Biotechnology. 2006; 81(4):505–510. https://doi.org/10.1002/jctb.1465

31. Batchelor GK. An Introduction to Fluid Dynamics. Cambridge: Cambridge University Press; 2000. Available from: http://ebooks.cambridge.org/ref/id/CBO9780511800955.

32. Oliphant TE. Python for Scientific Computing. Computing in Science & Engineering. 2007; 9(3):10–20. https://doi.org/10.1109/MCSE.2007.58

33. Limbach HJ, Arnold A, Mann BA, Holm C. ESPResSo—an extensible simulation package for research on soft matter systems. Computer Physics Communications. 2006; 174(9):704–727. https://doi.org/10.1016/j.cpc.2005.10.005

34. Roehm D, Arnold A. Lattice Boltzmann simulations on GPUs with ESPResSo. The European Physical Journal Special Topics. 2012; 210(1):89–100. https://doi.org/10.1140/epjst/e2012-01639-6

35. Sarker M, Chen XB. Modeling the Flow Behavior and Flow Rate of Medium Viscosity Alginate for Scaffold Fabrication With a Three-Dimensional Bioplotter. Journal of Manufacturing Science and Engineering. 2017; 139(8):081002. https://doi.org/10.1115/1.4036226

Supplementary material for the manuscript

Flow and hydrodynamic shear stress inside a printing needle during biofabrication

Sebastian J. Müller[1], Elham Mirzahossein[2], Emil Iftekhar[2], Christian Bächer[1], Stefan Schrüfer[3], Dirk W. Schubert[3], Ben Fabry[2] and Stephan Gekle[1]

[1]Biofluid Simulation and Modeling, Universität Bayreuth, Germany
[2]Biophysics Group, Friedrich-Alexander Universität Erlangen-Nürnberg, Germany
[3]Polymer Physics and Processing, Friedrich-Alexander Universität Erlangen-Nürnberg, Germany
Authors to whom correspondence should be addressed:
sjmueller@uni-bayreuth.de, stephan.gekle@uni-bayreuth.de

S-1. Theory

Our algorithm starts from an experimentally known viscosity-shear rate relation $\eta(\dot{\gamma})$ and interpolates it by a series of power-law functions. This interpolation is subsequently used for writing down a similar series of Navier-Stokes equations which are solved first for the shear rate and then for the velocity profile.

S-1.1. Viscosity model

The viscosity-shear rate relationship of the bioink, or any other generalized Newtonian fluid, can be approximated by a continuous, piecewise function

$$\eta\left(\dot{\gamma}\right) = \begin{cases} K_0\dot{\gamma}^{n_0-1} & 0 \leq \dot{\gamma} < \dot{\Gamma}_0 \\ \vdots & \\ K_i\dot{\gamma}^{n_i-1} & \dot{\Gamma}_{i-1} \leq \dot{\gamma} < \dot{\Gamma}_i \\ \vdots & \\ K_N\dot{\gamma}^{n_N-1} & \dot{\Gamma}_{N-1} \leq \dot{\gamma} < \infty \end{cases}, \tag{S-1}$$

as depicted in figure 1a of the main text. In every interval the viscosity-shear rate relation is described by a power-law model with a consistency parameter K_i having the physical unit $\mathrm{Pa\,s^{n_i}}$, and a dimensionless exponent n_i, according to the literature [1–7]. We note that the shear rate can also be understood as dimensionless quantity, normalized to a constant shear rate of $1\,\mathrm{s}^{-1}$ without changing its numerical value. Doing so, the consistency parameter can be interpreted as a reference viscosity with the more meaningful physical unit Pa s.
The i^{th} interval is bounded by the shear rates $\dot{\Gamma}_{i-1}$ and $\dot{\Gamma}_i$. The condition

$$K_i\dot{\Gamma}_i^{n_i-1} = K_{i+1}\dot{\Gamma}_i^{n_{i+1}-1} \tag{S-2}$$

ensures the continuity of (S-1) across the interval boundary $\dot{\Gamma}_i$ $(i = 0, \ldots, N-1)$. Since real fluids usually exhibit Newtonian behavior for zero and infinite shear rates, we take

$$n_0 = n_N = 1 \tag{S-3}$$

for the power-law exponents in the first and last interval.
We note that instead of the power-law interpolation, a linear interpolation would also be possible. However, since most bioinks show power-law shear thinning over a wide range of shear rates, a power-law interpolation is computationally more efficient when logarithmically-spaced shear rate intervals are used, as shown in figure 1a.

S-1.2. Determination of K_i and n_i

Starting from an experimentally known viscosity-shear rate relation $\tilde{\eta}\left(\dot{\gamma}\right)$ which can be given either as raw rheological data or as a viscosity model with known parameters

(e.g. [8, 9]) such as the Carreau-Yasuda model, the consistency indices K_i and exponents n_i in each interpolation interval are determined as follows. The lowest and highest consistency indices are fixed by eq. (S-3) as

$$K_0 = \tilde{\eta}\left(\dot{\Gamma}_0\right) \quad \text{and} \quad K_N = \tilde{\eta}\left(\dot{\Gamma}_{N-1}\right) \quad . \tag{S-4}$$

Since rheological data often spans multiple decades, we choose an equidistant partitioning of the interval $[\dot{\Gamma}_0, \dot{\Gamma}_{N-1}]$ on a logarithmic scale, as shown in figure 1a. Given the bounds of this interval and the number of interpolated points, the intermediate shear rates are given by

$$\dot{\Gamma}_i = \dot{\Gamma}_0 \left(\frac{\dot{\Gamma}_{N-1}}{\dot{\Gamma}_0}\right)^{\frac{i}{N-1}} \quad . \tag{S-5}$$

The parameters of the interpolating power-law functions $\eta_i(\dot{\gamma})$ are found by inserting the known viscosity values at the interval bounds. Thus, the following system of equations needs to be solved:

$$K_i \dot{\Gamma}_{i-1}^{n_i-1} = \tilde{\eta}\left(\dot{\Gamma}_{i-1}\right) \tag{S-6}$$

$$K_i \dot{\Gamma}_{i}^{n_i-1} = \tilde{\eta}\left(\dot{\Gamma}_{i}\right) \tag{S-7}$$

By division of the two equations, the power-law exponent is found to be

$$n_i = 1 + \log\left(\frac{\tilde{\eta}\left(\dot{\Gamma}_{i-1}\right)}{\tilde{\eta}\left(\dot{\Gamma}_i\right)}\right)\left(\log\left(\frac{\dot{\Gamma}_{i-1}}{\dot{\Gamma}_i}\right)\right)^{-1} \quad . \tag{S-8}$$

Multiplication of (S-6) by (S-7) gives an expression for the consistency index:

$$K_i = \sqrt{\tilde{\eta}\left(\dot{\Gamma}_{i-1}\right)\tilde{\eta}\left(\dot{\Gamma}_i\right)}\left(\dot{\Gamma}_{i-1}\dot{\Gamma}_i\right)^{\frac{1-n_i}{2}} \tag{S-9}$$

By inserting a functional form or raw data for $\tilde{\eta}(\dot{\gamma})$ into (S-8) and (S-9) the interpolation can be performed in the entire range of shear rates.

S-1.3. Governing equations

The Navier-Stokes equations to determine the flow field $\vec{u}$ read

$$\varrho\left[\frac{\partial \vec{u}}{\partial t} + (\vec{u}\cdot\boldsymbol{\nabla})\,\vec{u}\right] = -\boldsymbol{\nabla}p + \boldsymbol{\nabla}\cdot\left(\underline{\underline{\tau}}\right) + \vec{f} \quad , \tag{S-10}$$

with the fluid mass density ϱ, the pressure gradient $\boldsymbol{\nabla}p$, the viscous stress tensor $\underline{\underline{\tau}}$, and an external force term $\vec{f}$. The viscous stress tensor is related to the viscosity and the strain rate tensor $\underline{\underline{\varepsilon}}$ via

$$\underline{\underline{\tau}} = 2\eta(\dot{\gamma})\,\underline{\underline{\varepsilon}} \quad , \tag{S-11}$$

where the strain rate tensor is defined as

$$\underline{\underline{\varepsilon}} = \tfrac{1}{2}\left[\boldsymbol{\nabla}\vec{u} + (\boldsymbol{\nabla}\vec{u})^{\intercal}\right] \quad . \tag{S-12}$$

Here, $\boldsymbol{\nabla}\vec{u}$ denotes the dyadic product of the gradient operator and the velocity vector and $(\boldsymbol{\nabla}\vec{u})^{\intercal}$ its transpose. The shear rate can be obtained as invariant of the strain rate tensor, i. e.

$$\dot{\gamma} = \sqrt{2\sum_{\alpha,\beta}\varepsilon_{\alpha\beta}\varepsilon_{\alpha\beta}} \quad . \tag{S-13}$$

For a purely Newtonian fluid, the viscosity in (S-11) would be a constant.

S-1.3.1. Flow conditions. Analogously to the well-known Poiseuille flow of a Newtonian fluid [10, pp. 180 ff.], we assume a stationary, laminar, and pressure driven flow, with the velocity having only an axial component depending on the radial position. We consider a cylindrical channel and neglect entrance and exit effects. For the following derivation, a cylindrical coordinate system with a radial component r, an azimuthal component ϕ, and an axial component z, is employed. In these coordinates, the flow conditions read:

$$\vec{f} = \vec{0} \tag{S-14}$$

$$\frac{\partial\vec{u}}{\partial t} = \vec{0} \tag{S-15}$$

$$\frac{\partial\vec{u}}{\partial z} = \vec{0} \tag{S-16}$$

$$\frac{\partial\vec{u}}{\partial\phi} = \vec{0} \tag{S-17}$$

$$\vec{u}\,(r,\phi,z) = u\vec{e}_z \tag{S-18}$$

S-1.3.2. Constant pressure gradient. For a purely Newtionan fluid, the flow conditions (S-14)-(S-18) imply a spatially constant pressure gradient throughout the entire channel. In the following, we prove that the same holds for an arbitrary generalized Newtonian fluid. The strain rate tensor in cylindrical coordinates reads:

$$\underline{\underline{\varepsilon}} = \tfrac{1}{2}\begin{pmatrix} \underbrace{2\partial_r u_r}_{(S-18)_0} & \underbrace{\partial_r u_\phi + \frac{1}{r}\partial_\phi u_r - \frac{1}{r}u_\phi}_{(S-17),(S-18)_0} & \underbrace{\partial_z u_r}_{(S-18)_0} + \partial_r u_z \\ - & \underbrace{2\partial_\phi u_\phi + 2\frac{1}{r}u_r}_{(S-17),(S-18)_0} & \underbrace{\frac{1}{r}\partial_\phi u_z + \partial_z u_\phi}_{(S-17)_0} \\ - & - & \underbrace{2\partial_z u_z}_{(S-16)_0} \end{pmatrix} \tag{S-19}$$

where the notation $\partial_x = \frac{\partial}{\partial x}$ denotes a partial spatial derivative with respect to the coordinate x. The "$-$" signs indicate the symmetric components of the tensor. The

underbraced terms vanish due to the flow conditions. Thus, the viscous stress tensor reduces to a single component,

$$\tau_{rz} = \tau_{zr} = \eta\left(\dot{\gamma}\right) \frac{\partial u_z}{\partial r} \quad . \tag{S-20}$$

The components of the NSE yield:

$$\frac{\partial p}{\partial r} = 0 \qquad (r-\text{component}) \tag{S-21}$$

$$\frac{\partial p}{\partial \phi} = 0 \qquad (\phi-\text{component}) \tag{S-22}$$

$$\frac{\partial p}{\partial z} = \frac{1}{r}\frac{\partial}{\partial r}\left(r\tau_{rz}\right) \qquad (z-\text{component}) \tag{S-23}$$

This shows that the pressure gradient has only a z-component. By applying the derivative ∂_z again on the remaining z-component of the NSE, we obtain:

$$\partial_z^2 p = \partial_z \left[\frac{1}{r}\partial_r \left(r\eta\left(\dot{\gamma}\right)\partial_r u\right)\right] \tag{S-24}$$

$$= \frac{1}{r}\partial_r \left[r\partial_z \left(\eta\left(\dot{\gamma}\right)\partial_r u\right)\right] \tag{S-25}$$

$$= \frac{1}{r}\partial_r \left(r\eta\left(\dot{\gamma}\right)\partial_r \underbrace{\partial_z u}_{\overset{(S-17)}{=}0} + r\partial_r u \underbrace{\partial_z \eta\left(\dot{\gamma}\right)}_{\overset{(S-17)}{=}0} \right) = 0 \tag{S-26}$$

which shows that the pressure gradient is indeed constant and allows us to define

$$G := \frac{\partial p}{\partial z} = \frac{\Delta p}{L} \quad , \tag{S-27}$$

where $\Delta p = p_L - p_0 < 0$ is the pressure difference along a channel segment of length L. Applying the flow conditions, the Navier-Stokes equations reduce to the ordinary differential equation (1):

$$G = \frac{1}{r}\frac{\partial}{\partial r}\left(r\eta\left(\dot{\gamma}\right)\frac{\partial u}{\partial r}\right) \tag{S-28}$$

This equation is however still highly non-linear due to the dependency of $\eta\left(\dot{\gamma}\right)$ on $\partial_r u$ via the shear rate $\dot{\gamma}$ (cf. (S-31), (4)).

S-1.3.3. Ansatz and boundary conditions. Similar to the piecewise viscosity model in (S-1), we decompose the axial velocity $u\left(r\right)$ into intervals:

$$u\left(r\right) = \begin{cases} u_0\left(r\right) & 0 \le r < R_0 \\ \vdots & \\ u_i\left(r\right) & R_{i-1} \le r < R_i \\ \vdots & \\ u_N\left(r\right) & R_{N-1} \le r < \infty \end{cases} \tag{S-29}$$

as illustrated in figure 1b. The essential difference between (S-1) and (S-29) is that the interval boundaries are determined by shear rates $\dot{\Gamma}_i$ for the former and by radial positions R_i for the latter. While the interval boundaries for the viscosity $\dot{\Gamma}_i$ are an input quantity (see section S-1.2), the radial boundaries are determined *a posteriori* from the shear rate profile by the condition

$$\dot{\gamma}\left(R_i\right) = \dot{\Gamma}_i \tag{S-30}$$

as will be shown in (S-42) below. The shear rate as a function of the radial position $\dot{\gamma}\left(r\right)$ is given by the first derivative of the velocity with respect to the radial position, i. e.

$$\dot{\gamma}\left(r\right) = -\frac{\partial u\left(r\right)}{\partial r} \quad , \tag{S-31}$$

and can also be written in the same piecewise manner:

$$\dot{\gamma}\left(r\right) = \begin{cases} \dot{\gamma}_0\left(r\right) & 0 \leq r < R_0 \\ \vdots & \\ \dot{\gamma}_i\left(r\right) & R_{i-1} \leq r < R_i \\ \vdots & \\ \dot{\gamma}_N\left(r\right) & R_{N-1} \leq r < \infty \end{cases} \tag{S-32}$$

As for classical Poiseuille flow, we assume the common case of the velocity monotonically decreasing with the radial position. According to (S-31), the shear rate is therefore always positive. For $u\left(r\right)$ to be continuously differentiable and finite at the channel center, the piecewise definitions of the velocity and the shear rate must be equal at the intermediate points, R_i, i. e.

$$u_i\left(R_i\right) = u_{i+1}\left(R_i\right) \tag{S-33}$$

and

$$\dot{\gamma}_i\left(R_i\right) = \dot{\gamma}_{i+1}\left(R_i\right) \quad . \tag{S-34}$$

The flow shall further fulfill a no-slip boundary condition at the cylindrical channel wall at $r = A$, i. e.

$$u\left(A\right) = 0 \quad . \tag{S-35}$$

To ensure the continuous differentiability of the axially symmetric flow field, the flow must have a maximum at the channel center, $r = 0$. Therefore, the shear rate has to vanish at this point:

$$\dot{\gamma}\left(0\right) = 0 \tag{S-36}$$

S-1.4. Solution to the shear rate profile

Inserting the ansatz (S-29) and (S-32) into the Navier-Stokes equation (S-28) yields the following system of equations, (3) and (4), where $i \in \{0, \ldots, N\}$ denotes the intervals as above:

$$G = \frac{1}{r}\frac{\partial}{\partial r}\left(-rK_i\dot{\gamma}_i\left(r\right)^{n_i}\right) \tag{S-37}$$

$$\dot{\gamma}_i\left(r\right) = -\frac{\partial u_i\left(r\right)}{\partial r} \quad . \tag{S-38}$$

The first equation (S-37), (3), can be rearranged and integrated once to obtain

$$\dot{\gamma}_i\left(r\right) = \left(-\frac{Gr}{2K_i} - \frac{c_i}{K_i r}\right)^{\frac{1}{n_i}} \quad , \tag{S-39}$$

where the c_i are a set of integration constants that are determined next using the continuity conditions (S-34) and the boundary condition (S-36).

S-1.4.1. Determination of the integration constants of the shear rate profile. The integration constants c_i can be shown to be zero using the complete induction proof described in the following. The base clause, (S-39) for $i = 0$ with the boundary condition (S-36) gives

$$\dot{\gamma}_0\left(0\right) = \lim_{r\to 0}\left(-\frac{Gr}{2K_0} - \frac{c_0}{K_0 r}\right)^{\frac{1}{n_0}} \stackrel{!}{=} 0 \quad , \tag{S-40}$$

which is only fulfilled if the integration constant vanishes, thus, $c_0 = 0$.
Assuming that $c_i = 0$, c_{i+1} can be determined using the continuity condition (S-34),

$$\dot{\gamma}_i\left(R_i\right) = \dot{\gamma}_{i+1}\left(R_i\right) = \dot{\Gamma}_i \quad , \tag{S-41}$$

where the $\dot{\Gamma}_i$ are given. The equality $\dot{\Gamma}_i = \dot{\gamma}_i\left(R_i\right)$ yields an expression for the radial position R_i of the interfacial point between $\dot{\gamma}_i\left(r\right)$ and $\dot{\gamma}_{i+1}\left(r\right)$,

$$R_i = -\frac{2K_i\dot{\Gamma}_i^{n_i}}{G} \quad , \tag{S-42}$$

that can be inserted into the second part of (S-41) using (S-39):

$$\dot{\Gamma}_i = \left(-\frac{GR_i}{2K_{i+1}} - \frac{c_{i+1}}{K_{i+1}R_i}\right)^{\frac{1}{n_{i+1}}} \tag{S-43}$$

$$= \left(\frac{K_i}{K_{i+1}}\dot{\Gamma}_i^{n_i} + \frac{c_{i+1}G}{2K_{i+1}K_i\dot{\Gamma}_i^{n_i}}\right)^{\frac{1}{n_{i+1}}} \tag{S-44}$$

Employing the continuity condition of the viscosity model (S-2) gives an expression for the ratio of the consistency parameters, i. e.

$$K_i\dot{\Gamma}_i^{n_i-1} = K_{i+1}\dot{\Gamma}_i^{n_{i+1}-1} \tag{S-45}$$

$$\frac{K_i}{K_{i+1}} = \dot{\Gamma}_i^{n_{i+1}-n_i} \quad . \tag{S-46}$$

Inserting (S-46) into (S-44) finally yields

$$\dot{\Gamma}_i = \left(\dot{\Gamma}_i^{n_{i+1}} + \frac{c_{i+1} G}{2 K_{i+1} K_i \dot{\Gamma}_i^{n_i}} \right)^{\frac{1}{n_{i+1}}} \quad , \tag{S-47}$$

which is equal only if $c_{i+1} = 0$ thus completing the proof.
With that, the final form for the shear rate profile in the i^{th} interval is obtained as (cf. (5)):

$$\dot{\gamma}_i(r) = \left(-\frac{G}{2K_i} r \right)^{\frac{1}{n_i}} \tag{S-48}$$

Note that this solution reduces to the simple power-law model solution if the index i is dropped.

S-1.5. Solution to the velocity profile

The velocity profile is obtained by inserting (S-48), (5), into the second part of the system of differential equations (S-38), (4), and integrating over r:

$$\frac{\partial u_i(r)}{\partial r} = -\left(-\frac{G}{2K_i} r \right)^{\frac{1}{n_i}} \tag{S-49}$$

$$u_i(r) = -\left(-\frac{G}{2K_i} \right)^{\frac{1}{n_i}} \frac{n_i}{n_i + 1} r^{1+\frac{1}{n_i}} + \tilde{c}_i \tag{S-50}$$

The integration constants $\tilde{c}_i$ are determined next using the no-slip boundary condition (S-35) and the continuity conditions for the velocity field (S-33).

S-1.5.1. Determination of the integration constants of the velocity profile. Since the number of intervals of the viscosity model N is independent of the choice of the flow parameters, G and A, and this choice uniquely determines the R_i via (S-42), the outer channel boundary R is not necessarily located in the last interval of the velocity ansatz function $u_N(r)$. Instead, the radius of the channel lies in the k^{th} interval, i. e.

$$R_{k-1} \leq A \leq R_k \quad , \tag{S-51}$$

where $0 < k \leq N$. Intervals with $i > k$ whose boundaries R_i lie beyond the channel radius A have no physical significance and are disregarded in the following. Consequently, the no-slip boundary condition applies to the k^{th} interval:

$$u_k(A) = -\left(-\frac{G}{2K_k} \right)^{\frac{1}{n_k}} \frac{n_k}{n_k + 1} A^{1+\frac{1}{n_k}} + \tilde{c}_k \stackrel{!}{=} 0 \tag{S-52}$$

The integration constant can therefore easily be found as

$$\tilde{c}_k = \left(-\frac{G}{2K_k} \right)^{\frac{1}{n_k}} \frac{n_k}{n_k + 1} A^{1+\frac{1}{n_k}} \quad . \tag{S-53}$$

For $i < k$, the continuity condition for the velocity field (S-33) can be written as

$$-\left(-\frac{G}{2K_i}\right)^{\frac{1}{n_i}} \frac{n_i}{n_i+1} R_i^{1+\frac{1}{n_i}} + \tilde{c}_i = -\left(-\frac{G}{2K_{i+1}}\right)^{\frac{1}{n_{i+1}}} \frac{n_{i+1}}{n_{i+1}+1} R_i^{1+\frac{1}{n_{i+1}}} + \tilde{c}_{i+1} \quad . \tag{S-54}$$

Assuming that $\tilde{c}_{i+1}$ is known and rearranging this equation for $\tilde{c}_i$ yields

$$\tilde{c}_i = \tilde{c}_{i+1} - R_i \left[\underbrace{\left(-\frac{G}{2K_{i+1}}\right)^{\frac{1}{n_{i+1}}} R_i^{\frac{1}{n_{i+1}}}}_{=\,\dot{\gamma}_{i+1}(R_i)\,=\,\dot{\Gamma}_i} \frac{n_{i+1}}{n_{i+1}+1} - \underbrace{\left(-\frac{G}{2K_i}\right)^{\frac{1}{n_i}} R_i^{\frac{1}{n_i}}}_{=\,\dot{\gamma}_i(R_i)\,=\,\dot{\Gamma}_i} \frac{n_i}{n_i+1} \right] \quad , \tag{S-55}$$

where the underbraced terms can be identified as the shear rates at the interfacial position which are equal by the continuity conditions (S-34). Hence,

$$\tilde{c}_i = \tilde{c}_{i+1} - R_i \dot{\Gamma}_i \left(\frac{n_{i+1}}{n_{i+1}+1} - \frac{n_i}{n_i+1} \right) \quad . \tag{S-56}$$

Finally, inserting the expression for the known outermost integration constant, $\tilde{c}_k$, the interior integration constants can be determined as

$$\tilde{c}_i = \tilde{c}_k - \sum_{j=i}^{k-1} R_j \dot{\Gamma}_j \left(\frac{n_{j+1}}{n_{j+1}+1} - \frac{n_j}{n_j+1} \right) \quad . \tag{S-57}$$

Combining (S-50), (S-53) and (S-57), the velocity profile in the i^{th} interval is given by (6):

$$\begin{aligned} u_i(r) = &-\left(-\frac{G}{2K_i}\right)^{\frac{1}{n_i}} \frac{n_i}{n_i+1} r^{1+\frac{1}{n_i}} + \left(-\frac{G}{2K_k}\right)^{\frac{1}{n_k}} \frac{n_k}{n_k+1} A^{1+\frac{1}{n_k}} \\ &- \sum_{j=i}^{k-1} R_j \dot{\Gamma}_j \left(\frac{n_{j+1}}{n_{j+1}+1} - \frac{n_j}{n_j+1} \right) \end{aligned} \tag{S-58}$$

S-1.6. Calculation of averages

In the following, we derive mathematical expressions for the flow rate as well as the average shear rate, viscosity, and shear stress. The flow rate or, equivalently, the average flow velocity determines the printing speed in 3D bioprinting processes. The average shear rate and shear stress can be used to estimate cell damage during printing [7, 11].

S-1.6.1. Average velocity and flow rate. The cross-sectional average of the velocity field is given by

$$\overline{u} = \frac{1}{\pi A^2} \int_0^{2\pi} \mathrm{d}\phi \int_0^A \mathrm{d}r \, r u(r) \quad . \tag{S-59}$$

The first integral can be evaluated and gives a factor 2π, the second integral is split into the intervals:

$$\overline{u} = \frac{2}{A^2}\left[\int_0^{R_0} \mathrm{d}r\, r u_0\left(r\right) + \sum_{i=1}^{k-1}\int_{R_{i-1}}^{R_i} \mathrm{d}r\, r u_i\left(r\right) + \int_{R_{k-1}}^{A} \mathrm{d}r\, r u_k\left(r\right)\right] \tag{S-60}$$

Abbreviating the prefactors in (S-50), i. e.

$$u_i\left(r\right) = a_i r^{1+\frac{1}{n_i}} + \tilde{c}_i \quad , \tag{S-61}$$

with

$$a_i = -\left(-\frac{G}{2K_i}\right)^{\frac{1}{n_i}} \frac{n_i}{n_i+1} \quad , \tag{S-62}$$

the average velocity is found to be:

$$\begin{aligned}\overline{u} = \frac{2}{A^2}\Bigg[&\frac{a_0}{3+\frac{1}{n_0}} R_0^{3+\frac{1}{n_0}} + \frac{\tilde{c}_0}{2} R_0^2 + \sum_{i=1}^{k-1} \frac{a_i}{3+\frac{1}{n_i}}\left(R_i^{3+\frac{1}{n_i}} - R_{i-1}^{3+\frac{1}{n_i}}\right) \\ &+ \sum_{i=1}^{k-1} \frac{\tilde{c}_i}{2}\left(R_i^2 - R_{i-1}^2\right) + \frac{a_k}{3+\frac{1}{n_k}}\left(A^{3+\frac{1}{n_k}} - R_{k-1}^{3+\frac{1}{n_k}}\right) + \frac{\tilde{c}_k}{2}\left(A^2 - R_{k-1}^2\right)\Bigg]\end{aligned} \tag{S-63}$$

The flow rate is given by

$$\Omega = \pi A^2 \overline{u} \quad . \tag{S-64}$$

S-1.6.2. Average shear rate. The same procedure as above can be applied to find the average shear rate. With (S-48) shortened to

$$\dot{\gamma}_i\left(r\right) = b_i r^{\frac{1}{n_i}} \quad , \tag{S-65}$$

the average shear rate is given by:

$$\overline{\dot{\gamma}} = \frac{2}{A^2}\left[\frac{b_0}{2+\frac{1}{n_0}} R_0^{2+\frac{1}{n_0}} + \sum_{i=1}^{k-1} \frac{b_i}{2+\frac{1}{n_i}}\left(R_i^{2+\frac{1}{n_i}} - R_{i-1}^{2+\frac{1}{n_i}}\right) + \frac{b_k}{2+\frac{1}{n_k}}\left(A^{2+\frac{1}{n_k}} - R_{k-1}^{2+\frac{1}{n_k}}\right)\right] \tag{S-66}$$

S-1.6.3. Average viscosity. The viscosity field, $\eta\left(r\right)$, is calculated by inserting the shear rate field from (S-48) into the power-law definitions of the respective interpolation interval in (S-1). Thus,

$$\eta_i\left(r\right) = K_i\left(\dot{\gamma}_i\left(r\right)\right)^{n_i-1} = K_i\left(-\frac{G}{2K_i} r\right)^{1-\frac{1}{n_i}} \quad , \tag{S-67}$$

which can be shortened to

$$\eta_i(r) = d_i r^{1-\frac{1}{n_i}} \quad . \tag{S-68}$$

Using the same procedure as above, the integral in the i^{th} interval yields

$$\int_{R_{i-1}}^{R_i} \mathrm{d}r\, r\eta_i(r) = \frac{d_i}{3-\frac{1}{n_i}} \left(R_i^{3-\frac{1}{n_i}} - R_{i-1}^{3-\frac{1}{n_i}} \right) \tag{S-69}$$

if $n_i \neq \frac{1}{3}$ and

$$\int_{R_{i-1}}^{R_i} \mathrm{d}r\, r\eta_i(r) = d_i \int_{R_{i-1}}^{R_i} \mathrm{d}r\, r^{-1} = d_i \ln\left(\frac{R_i}{R_{i-1}}\right) \tag{S-70}$$

if $n_i = \frac{1}{3}$. The average viscosity for our model is therefore given by

$$\overline{\eta} = \frac{2}{A^2} \left[\int_0^{R_0} \mathrm{d}r\, r\eta_0(r) + \sum_{i=1}^{k-1} \int_{R_{i-1}}^{R_i} \mathrm{d}r\, r\eta_i(r) + \int_{R_{k-1}}^{A} \mathrm{d}r\, r\eta_k(r) \right] \quad , \tag{S-71}$$

where the integrals are chosen as (S-69) or (S-70) according to n_i. ‡

S-1.6.4. Average shear stress. The radial profile of the shear stress is given as the product of the shear rate field (S-48) and the viscosity field. The latter is calculated by inserting the shear rate field from (S-48) into the power-law definitions of the respective interpolation interval in (S-1):

$$\eta_i(r) = K_i \left(\dot{\gamma}_i(r)\right)^{n_i - 1} \tag{S-72}$$

The shear stress profile is therefore obtained as

$$\begin{aligned} \sigma_i(r) &= \dot{\gamma}_i(r)\, \eta_i(r) = K_i \left(\dot{\gamma}_i(r)\right)^{n_i} \\ &= -\tfrac{1}{2} G r = \sigma(r) \quad , \end{aligned} \tag{S-73}$$

where the index i can be dropped since it is independent of the viscosity interpolation. This linear relationship of shear stress and radial position is well-known for power-law fluids [11]. Its average is found by simply solving one integral that yields:

$$\overline{\sigma} = \frac{2}{A^2} \int_0^A \mathrm{d}r\, r\sigma(r) = -\frac{GA}{3} \tag{S-74}$$

‡ Note that in the inner-most interval with R_0 as its right boundary the shear rate is always close to zero and thus the fluid is Newtonian with $n_0 = 1$ (see (S-3)) such that the mathematically undefined situation of (S-70) with $R_{i-1} = 0$ is excluded.

S-1.7. Global analytical solution for a simplified CY model

In order to validate the algorithm presented above according to the procedure described in section 2 of the manuscript, we calculate a global mathematical solution to the Navier-Stokes equation (S-28), (1), for a simplified Carreau-Yasuda model. In the following, we derive an analytical solution for the flow profiles of a CY model (cf. (9)) with the following simplification:

$$\begin{aligned} \eta_\infty &= 0 \\ a_1 = a_2 &= 1 \end{aligned} \tag{S-75}$$

The viscosity as a function of the shear rate is therefore given as (cf. (8))

$$\tilde{\eta}\left(\dot{\gamma}\right) = \frac{\eta_0}{1 + K\dot{\gamma}} \quad . \tag{S-76}$$

Using the same assumptions as in section S-1.3.1, the NSE yields:

$$G = \frac{1}{r}\frac{\partial}{\partial r}\left(-r\frac{\eta_0\dot{\gamma}}{1 + K\dot{\gamma}}\right) \tag{S-77}$$

After a first integration and rearrangement of the equations one obtains

$$\dot{\gamma}\left(r\right) = \frac{-\frac{Gr}{2} - \frac{c_1}{r}}{\eta_0 + \frac{KGr}{2} + \frac{Kc_1}{r}} \tag{S-78}$$

and application of boundary condition (S-36) determines the integration constant as $c_1 = 0$. Therefore, the shear rate profile is given as:

$$\dot{\gamma}\left(r\right) = \frac{-\frac{Gr}{2}}{\eta_0 + \frac{KGr}{2}} = -\frac{1}{\frac{2\eta_0}{Gr} + K} \tag{S-79}$$

Inserting this result into (S-38) and integrating the resulting equation gives the velocity profile:

$$\begin{aligned} u\left(r\right) &= -\int \mathrm{d}r\, \dot{\gamma}\left(r\right) \\ &= \frac{r}{K} - \frac{2\eta_0}{GK^2}\ln\left(\frac{2\eta_0}{G} + Kr\right) + c_2 \end{aligned} \tag{S-80}$$

The second integration is easily found by applying the no-slip boundary condition (S-35). Thus, the velocity profile is given by:

$$u\left(r\right) = \frac{r - A}{K} + \frac{2\eta_0}{GK^2}\ln\left(\frac{\frac{2\eta_0}{G} + KA}{\frac{2\eta_0}{G} + Kr}\right) \tag{S-81}$$

S-1.8. Estimate of force and deformation experienced by flowing cells

In this section, we provide a simple approach to estimate the force sensed by a cell and its resulting deformation during printing.
Both quantities depend on the radial position r at which the cell transitions through the channel. Considering, in a first approximation, the cell as a sphere with radius R_c, the shear force acting on it is given by the surface integral of the shear stress over the sphere. Due to the linearity of the shear stress with the radial position, and as long the cell is small compared to the channel, the force is obtained as the product of the surface area and the shear stress at the radial position of the sphere center, as detailed next.
With the shear stress given in (S-73), the shear force acting on the cell is obtained as:

$$\begin{aligned} F_z &= \int_0^{2\pi}\int_0^{\pi} \sigma\left(R_{\text{surface}}\right) R_c^2 \sin\theta \,\mathrm{d}\theta \;\mathrm{d}\phi \;= 2\pi R_c^2 \int_0^{\pi} \sigma\left(r + R_c\cos\theta\right)\sin\theta \,\mathrm{d}\theta \\ &= 2\pi R_c^2 \left(-\frac{G}{2}\right)\left[\underbrace{\int_0^{\pi} r\sin\theta\,\mathrm{d}\theta}_{=2r} + \underbrace{\int_0^{\pi} R_c\cos\theta\sin\theta\,\mathrm{d}\theta}_{=0}\right] = 4\pi R_c^2\left(-\frac{G}{2}r\right) \\ &= A_{\text{cell}}\cdot\sigma\left(r\right) \end{aligned} \tag{S-82}$$

The result is depicted in figure S-1a.
Another critical quantity is the cell deformation, which can be approximated using the shear stress and the mechanical properties of the cell. As a rough estimate, we assume the cell to behave linearly elastic with the stress–strain relationship given as

$$\varepsilon\left(r\right) = \frac{\sigma\left(r\right)}{E} \quad , \tag{S-83}$$

where the strain ε quantifies the relative stretching of the cell. The Young's modulus E is chosen as 1 kPa to 10 kPa to cover the typical range of stiffness for cells [13]. This leads to significant deformations as shown in figure S-1b which reiterates the importance of hydrodynamic shear forces in bioprinting.

Figure S-1. (a) The force F acting on cells as radial function according to (S-82). (b) The strain according to (S-83) as a deformation measure for a linear elastic cell. The corresponding flow profile is shown in fig. 3. We note that the assumption of linear elasticity predicts relatively large deformations, which would not be the case for a more realistic, strain-hardening behavior.

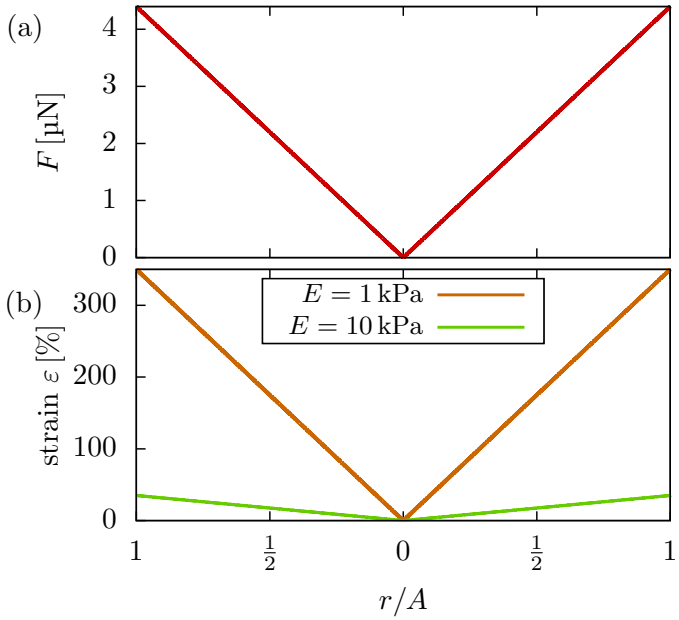

S-1.9. Inclusion of wall-slip effects

Wall-slip effects are sometimes reported, especially for fluids exhibiting non-Newtonian behavior [12] or highly hydrophobic channel coatings. The general approach to include a velocity slip at a wall is to allow for a finite tangential velocity at this point or, equivalently, to shift (in the calculations) the channel wall further outwards by a distance known as the slip length. It is thus straightforward to incorporate slip effects into our calculations if the slip length is known.
Alternatively, if the slip velocity next to the wall is known instead of the slip length, simply shifting upwards the computed no-slip velocity profile by a constant value represents a very good approximation. The shear rate would stay unchanged, and likewise the viscosity and the shear stress. Therefore, the inclusion of slip effects in our algorithm would be unproblematic.

S-2. Additional experimental validation of the algorithm

S-2.1. Additional experiments

In this section, we provide more validation to our algorithm with experimental measurements. Using the same approach as detailed in 2.3 of the manuscript, we performed velocity profile measurements of 2 % alginate at 100, 200, and 300 kPa, of 3 % alginate at 300, 400, and 500 kPa, and 3 % chitosan at 300, and 400 kPa. These measurements as well as the velocity profiles calculated using our Lattice Boltzmann method are depicted in figure S-2, showing good agreement. Since the pressure drop in the connectors and tubings is unknown but depends on the rheology of the hydrogel, we assume a constant pressure drop before the microchannel of 21 % for 2 % alginate, 10 % for 3 % alginate, and 23 % for 3 % chitosan, respectively. Additionally, we measured the flow profile of 3 % alginate in a rectangular microchannel with 1000 µm × 200 µm cross section. Due to limitations of the field of view of the microscope, less than one half of the channel could be focused during the measurements. In figure S-3, the mirrored experimentally measured velocity profile is shown in comparison to our Lattice Boltzmann calculations. Due to connectors and tubing with a diameter of approximately the size of the microchannel, the pressure drop of 48 % is reasonable.

S-2.2. Error quantification

In the following, we present an error calculation for the different flow experiments. First, we calculate an averaged velocity profile for the measurements as well as our calculations by averaging the data in a given d-interval. For the square channel, we choose a bin width of $d_{\mathrm{bin}} = 7.31\,\mu\mathrm{m}$ (corresponding to $N_{\mathrm{bins}} = 26$ bins in the range of $d = -95\,\mu\mathrm{m}$ to $95\,\mu\mathrm{m}$), for the rectangular channel $d_{\mathrm{bin}} = 16.3\,\mu\mathrm{m}$ (corresponding to $N_{\mathrm{bins}} = 26$ bins

Figure S-2. Experimentally measured velocity profiles in a 190 µm × 190 µm microchannel in comparison to numerical results using the Lattice Boltzmann method. (a, c, e) 2 % alginate at 100, 200, and 300 kPa. (b, d, f) 3 % alginate at 300, 400, and 500 kPa. (g, h) 3 % chitosan at 300 and 400 kPa.

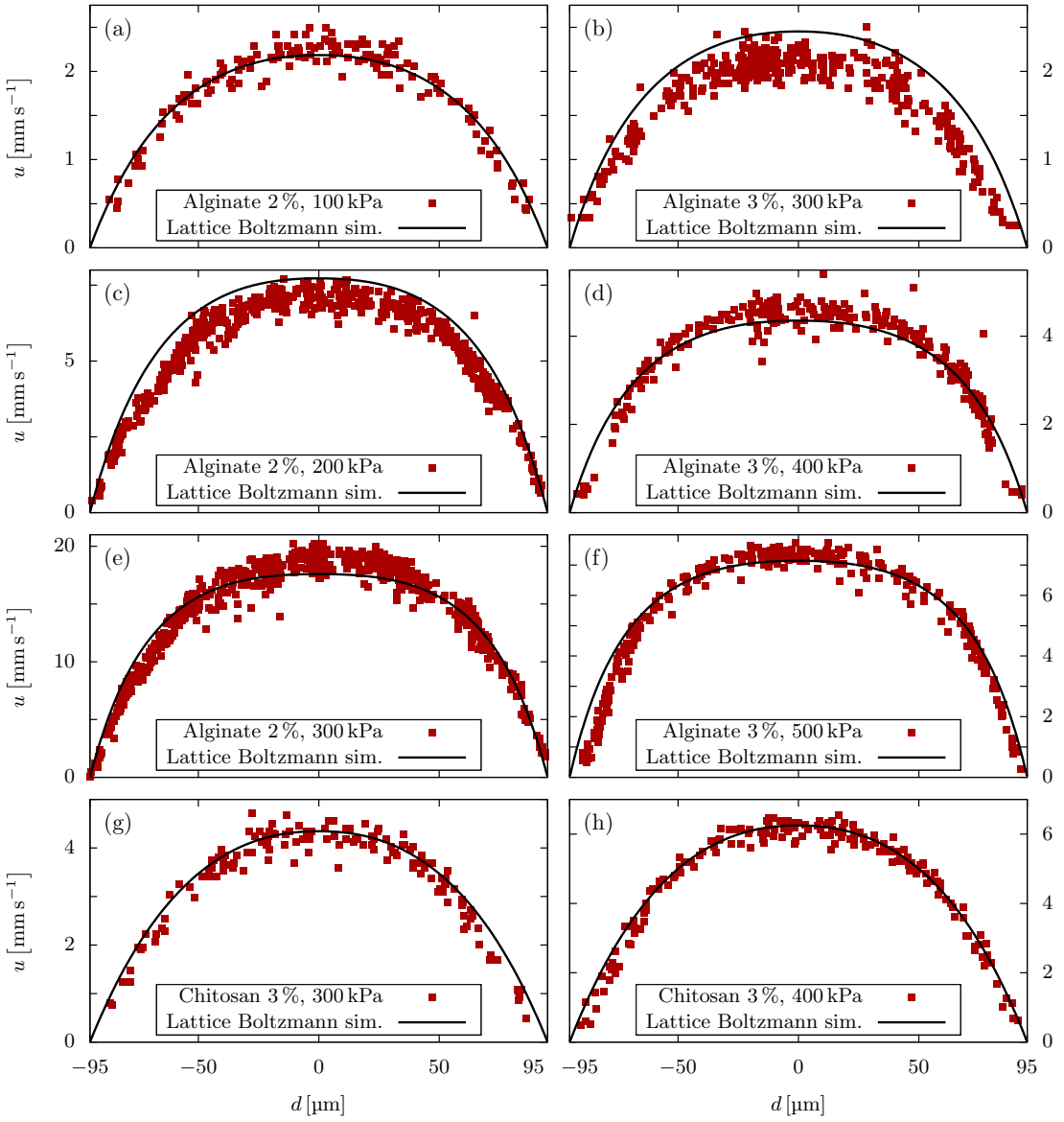

in the range of $d = 75\,\mu\text{m}$ to $500\,\mu\text{m}$). The average velocity in each bin is computed by

$$\overline{u}_i = \frac{1}{N_i} \sum_{k=1}^{N_i} u_k \quad , \tag{S-84}$$

Figure S-3. Experimentally measured velocity profiles of 3 % alginate at 400 and 500 kPa in a 1 mm × 200 µm microchannel in comparison to numerical results using the Lattice Boltzmann method. The experimental data is mirrored with respect to the channel center.

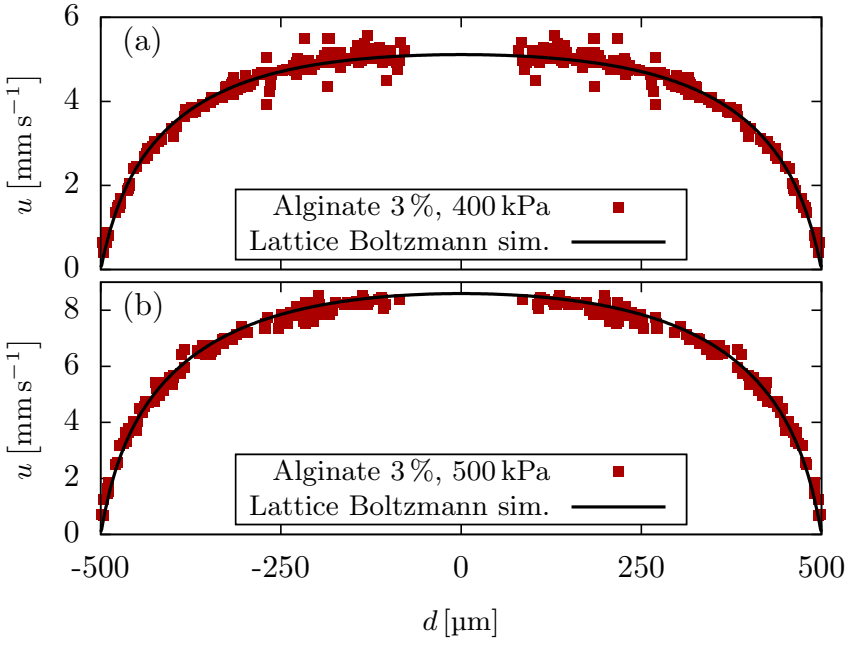

where N_i is the number of data points in the i-th bin. Using this approach, we additionally calculate the standard deviation of the data from the average value as

$$\sigma_{u,i} = \left(\frac{1}{N_i - 1} \sum_{k=1}^{N_i} (u_k - \overline{u}_i)^2 \right)^{\frac{1}{2}} \quad . \tag{S-85}$$

Using the averaged profiles, we calculate the relative error between measurement and Lattice Boltzmann computation as:

$$\epsilon = \left(\frac{1}{N_{\text{bins}}} \sum_{k=1}^{N_{\text{bins}}} \frac{\left(\overline{u}_k^{\text{Exp}} - \overline{u}_k^{\text{LB}} \right)^2}{\left(\overline{u}_{\text{max}}^{\text{LB}} \right)^2} \right)^{\frac{1}{2}} \tag{S-86}$$

The averaged profiles with a range of $\pm\sigma_{u,i}$ are shown in figure S-4 for the square microchannel and in figure S-5 for the rectangular microchannel, where we find relative errors in the range of $\epsilon = 3.3\,\%$ to $13.5\,\%$, and $\epsilon = 2\,\%$, respectively.

Figure S-4. Averaged profiles from figure S-2. The gray area indicates the range of one standard deviation from the mean curve. ϵ gives the relative error calculated according to (S-86).

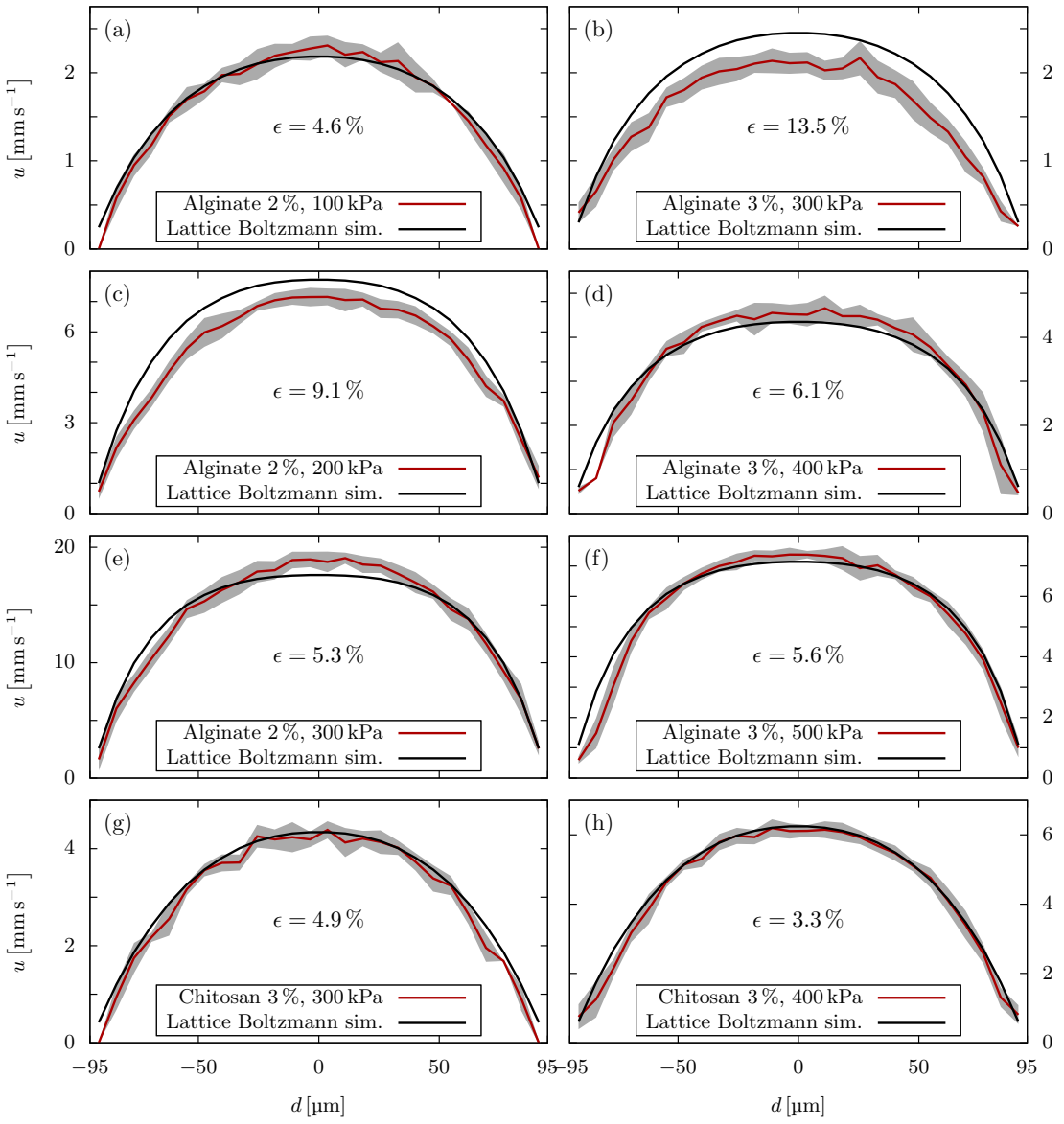

Figure S-5. Averaged profiles from figure S-3. The gray area indicates the range of one standard deviation from the mean curve. ϵ gives the relative error calculated according to (S-86).

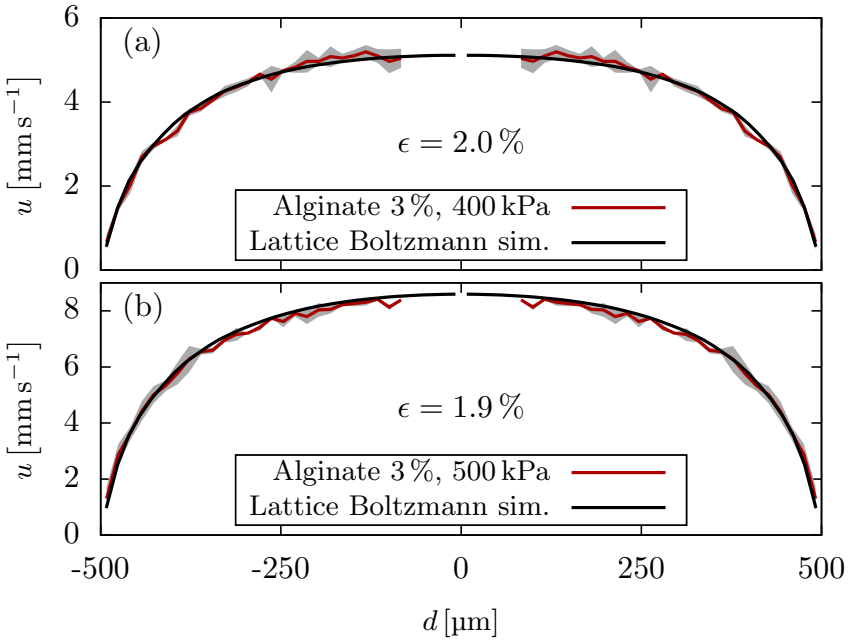

S-3. Computational procedure and user guide

This section describes the structure and usage of the Python classes, found in the Supplementary Material, that implement the presented algorithm for the Carreau-Yasuda model. The first part gives an overview of the four implemented Python classes. The second part provides a short user guide explaining how to use the classes for flow profile calculations. Note that their usage requires a Python (version 2 or 3) installation [14, 15]. The use of a Python IDE, e. g. Spyder [16], Thonny [17] or PyCharm [18], is optional but can be advantageous. The coloring in the code examples is the following: `blue` denotes classes, `green` denotes variables, and `gray` means a comment.
For the Carreau-Yasuda model [19] the viscosity is given by

$$\tilde{\eta}\left(\dot{\gamma}\right) = \tilde{\eta}_\infty + \frac{\tilde{\eta}_0 - \tilde{\eta}_\infty}{\left[1 + \left(K\dot{\gamma}\right)^{a_1}\right]^{\frac{a_2}{a_1}}} \quad , \tag{S-87}$$

where $\tilde{\eta}_0$ and $\tilde{\eta}_\infty$ are the viscosities in the limit of zero and infinite shear rates and K is a time constant with the unit s. Its inverse, $K^{-1} = \dot{\gamma}_c$, is sometimes referred to as *corner shear rate* and determines the transition to the zero-shear Newtonian plateau. The exponents a_1 and a_2 determine the shape of the transition between the zero-shear Newtonian plateau and the power-law region as well as the power-law behavior.

S-3.1. Overview of Python classes

The tool uses four classes that hold the input parameters, perform the calculations and save or plot output data. They can be found in the file `CYprofiles.py`. The four classes are:

(i) `Analytical_Viscosity()`: instances of this class hold the parameters of the Carreau-Yasuda model and can calculate the viscosity for a given shear rate according to (S-87).

(ii) `Interpolation()`: instances of this class perform the interpolation of a given `Analytical_Viscosity()` in a provided range of shear rates using the partitioning described in section S-1.2.

(iii) `Printing_Parameters()`: instances of this class hold the printing parameters, i.e. the nozzle radius and the pressure gradient or the flow rate.

(iv) `Profiles()`: instances of this class perform the calculation of the velocity, shear rate, and viscosity profile for given `Interpolation()` and `Printing_Parameters()` according to the presented algorithm. If a flow rate is provided, the corresponding pressure gradient is calculated iteratively to match the given flow rate.

S-3.2. User guide

This section is meant to serve as an explanatory tutorial for our Python tool. It will cover the two main steps necessary for calculating a flow profile: the viscosity

interpolation according to section S-1.2 and the profile calculation according to the presented algorithm. The following code examples can be found in the file `tutorial.py`.

Step 1 - Performing the interpolation Starting point for the viscosity interpolation is the Carreau-Yasuda model. After fitting rheological data, the values of its parameters in (S-87) are known. The `Analytical_Viscosity()` is then initialized by:

```
# initialize variables
eta0     =  1.0e2    ≙  η̃_0      [Pa s]
etainf   =  1.0e-3   ≙  η̃_∞      [Pa s]
K        =  1.0e-3   ≙  K        [s]
a1       =  0.3      ≙  a_1
a2       =  0.9      ≙  a_2

# initialize Analytical_Viscosity instance
analytical = Analytical_Viscosity( eta0=eta0, etainf=etainf,K=K,a1=a1,a2=a2 )
```

To perform the interpolation, the range of shear rates to interpolate and the number of (power-law) intervals is required:

```
# initialize variables
gamma0     =  1.0e-6   ≙  Γ̇_0      [s^-1]
gammaN     =  1.0e6    ≙  Γ̇_{N-1}  [s^-1]
Ninterpol  =  100      ≙  N - 1

# initialize Interpolation instance
interpol= Interpolation(gamma0=gamma0, gammaN=gammaN,
  Ninterpol=Ninterpol, analytical=analytical)
```

The calculation is then simply performed by executing

```
interpol.calculate_interpolation()
```

and the interpolation can be checked by plotting the calculated data via

```
interpol.plot_interpolation()
```

.

To save the viscosity interpolation, one can use

```
interpol.save_interpolation(file)
```

to save the data in viscosity-shear rate format and

```
interpol.save_interpolation_parameters(file)
```

to save the power-law parameters for all intervals in a file.

Step 2 - Calculating the flow profile Once the interpolation is completed, the next step is the definition of the printing parameters, i. e. the channel radius and the pressure gradient. This is done by:

```
# initialize variables
rchannel   =  1.0e-4  ≙  A   [m]
pgrad      =  -1.0e7  ≙  G   [Pa m^-1]

# initialize Printing_Parameters instance
printparams = Printing_Parameters(
  pressureGradient=pgrad, channelRadius=rchannel)
```

To calculate the radial profiles for the velocity (in $\mathrm{m\,s^{-1}}$), the shear rate (in $\mathrm{s^{-1}}$), and the viscosity (in $\mathrm{Pa\,s}$), the `Profiles()` class is initialized with printing parameters and an interpolation by

```
# initialize Profiles instance
fluidprofiles = Profiles(
  interpolation=interpol, printingParameters=printparams)
```

Finally, the calculation is performed by executing

```
fluidprofiles.calculate_profiles()
```

and the data can be plotted using the following methods:

```
fluidprofiles.plot_velocity()
fluidprofiles.plot_shearrate()
fluidprofiles.plot_shearstress()
fluidprofiles.plot_viscosity()
```

The data for all calculated fields is saved to a file with

```
fluidprofiles.save_profiles(file)
```

and

```
fluidprofiles.save_averages(file)
```

for the averaged quantities, respectively.
In the case of an imposed flow rate, i. e. if the pressure gradient is unknown, our tool automatically computes the corresponding pressure gradient necessary for the profile calculation. To do so, solely the initialization of the printing parameters changes as follows:

```
# initialize variables
rchannel   =  1.0e-4  ≙  A   [m]
flowrate   =  1.0e-9  ≙  Ω   [m^3 s^-1]
```

```
# initialize Printing_Parameters instance
printparams = Printing_Parameters(
  flowrate=flowrate, channelRadius=rchannel)
```

S-4. Lattice Boltzmann algorithm for generalized Newtonian fluids

This section briefly summarizes the Lattice Boltzmann method and the extension we added to the open-source package ESPResSo [20]. For an introduction into the Lattice Boltzmann method we refer the interested reader to the book by Krüger et al.[21]. The Lattice Boltzmann equation for the multiple relaxation time scheme used in ESPResSo reads:

$$f_i\left(\vec{x}+\vec{c}_i\Delta t, t+\Delta t\right) - f_i\left(\vec{x},t\right) = \sum_{j=0}^{18} \left(\underline{\underline{M}}^{-1}\underline{\underline{\omega}}\,\underline{\underline{M}}\right)_{ij}\left(f_j\left(\vec{x},t\right) - f_i^{\mathrm{eq}}\left(\vec{x},t\right)\right) \tag{S-88}$$

It describes the collision and streaming of the population distribution f_i $(i = 0, \ldots, 18)$ during one time step Δt. Here, $\vec{c}_i$ are the discretized lattice velocities, $\underline{\underline{M}}$ denotes transformation matrix that maps the populations onto moment space, $\underline{\underline{\omega}}$ is the diagonal relaxation frequency matrix, and f_i^{eq} denote the equilibrium population distributions. The relaxation frequency for the shear moments ω_{S} is related to the dynamic viscosity of the fluid via [22]

$$\eta = \varrho c_s^2 \left(\frac{1}{\omega_{\mathrm{S}}} - \tfrac{1}{2}\right)\Delta t \quad , \tag{S-89}$$

with the fluid mass density ϱ and the lattice speed of sound c_s. The calculation of the viscosity according to the rheological model requires the local shear rate at each lattice node. Chai *et al* [22] showed that the local strain rate tensor can be obtained from the populations by

$$\varepsilon_{\alpha\beta} = -\frac{1}{2\varrho c_s^2 \Delta t}\sum_{i,j=0}^{18}\left[\left(\vec{c}_i\right)_\alpha\left(\vec{c}_i\right)_\beta\left(\underline{\underline{M}}^{-1}\underline{\underline{\omega M}}\right)_{ij}\left(f_j\left(\vec{x},t\right) - f_i^{\mathrm{eq}}\left(\vec{x},t\right)\right)\right] \quad . \tag{S-90}$$

The shear rate is then obtained as invariant of the strain rate tensor according to (S-13). From the local shear rate, the viscosity according to the rheological model and the local relaxation time according to (S-89) are computed at each lattice node and updated in every time step.

In order to ensure simulation stability, we choose the time step globally according to Krüger *et al* [21, p. 273] as

$$\Delta t = c_s^2\left(\tau - \tfrac{1}{2}\right)\frac{\Delta x^2}{\nu^\star} = \frac{\Delta x^2}{6\nu^\star} \quad , \tag{S-91}$$

with $c_s^2 = \frac{1}{3}$, a global relaxation parameter $\tau = 1$, and a reference kinematic viscosity $\nu^\star$. The latter is provided, for instance, by the upper Newtonian viscosity plateau of

the corresponding CY model.
At the boundary of the cylindrical channel a bounce-back algorithm is applied to realize a no-slip boundary condition. The flow is driven by a pressure gradient along the z-direction, which is realized as external force density in the algorithm.

References

[1] Blaeser A, Duarte Campos D F, Puster U, Richtering W, Stevens M M and Fischer H 2015 *Advanced Healthcare Materials* **5** 326–333 ISSN 2192-2640

[2] Fu T, Carrier O, Funfschilling D, Ma Y and Li H Z 2016 *Chemical Engineering & Technology* **39** 987–992 ISSN 09307516 URL http://doi.wiley.com/10.1002/ceat.201500620

[3] Fyrippi I, Owen I and Escudier M 2004 *Flow Measurement and Instrumentation* **15** 131–138 ISSN 0955-5986

[4] Ning L, Betancourt N, Schreyer D J and Chen X 2018 *ACS Biomaterials Science & Engineering* **4** 3906–3918 ISSN 2373-9878, 2373-9878 URL http://pubs.acs.org/doi/10.1021/acsbiomaterials.8b00714

[5] Ruschak K J and Weinstein S J 2014 *Polymer Engineering & Science* **54** 2301–2309 ISSN 00323888 URL http://doi.wiley.com/10.1002/pen.23782

[6] Tian X Y, Li M G, Cao N, Li J W and Chen X B 2009 *Biofabrication* **1** 045005 ISSN 1758-5082

[7] Snyder J, Rin Son A, Hamid Q, Wang C, Lui Y and Sun W 2015 *Biofabrication* **7** 044106–17

[8] Escudier M, Gouldson I, Pereira A, Pinho F and Poole R 2001 *Journal of Non-Newtonian Fluid Mechanics* **97** 99–124 ISSN 03770257 URL http://linkinghub.elsevier.com/retrieve/pii/S0377025700001786

[9] Wu Q, Therriault D and Heuzey M C 2018 *ACS Biomaterials Science & Engineering* **4** 2643–2652 ISSN 2373-9878, 2373-9878 URL http://pubs.acs.org/doi/10.1021/acsbiomaterials.8b00415

[10] Batchelor G K 2000 *An Introduction to Fluid Dynamics* (Cambridge: Cambridge University Press) ISBN 978-0-511-80095-5 URL http://ebooks.cambridge.org/ref/id/CBO9780511800955

[11] Paxton N, Smolan W, Böck T, Melchels F, Groll J and Jüngst T 2017 *Biofabrication* **9** 044107 ISSN 1758-5090

[12] Sarker M and Chen X B 2017 *Journal of Manufacturing Science and Engineering* **139** 081002 ISSN 1087-1357, 1528-8935

[13] Yokokura T, Nakashima Y, Yonemoto Y, Hikichi Y and Nakanishi Y 2017 *International Journal of Engineering Science* **114** 41–48 ISSN 00207225

[14] Oliphant T E 2007 *Computing in Science & Engineering* **9** 10–20 ISSN 1521-9615

[15] 2019 Welcome to Python.org URL https://www.python.org/

[16] 2019 Spyder Website URL https://www.spyder-ide.org/

[17] 2019 Thonny, Python IDE for beginners URL https://thonny.org/

[18] 2019 PyCharm: the Python IDE for Professional Developers by JetBrains URL https://www.jetbrains.com/pycharm/

[19] Carreau P J 1972 *Transactions of the Society of Rheology* **16** 99–127 ISSN 0038-0032 URL http://sor.scitation.org/doi/10.1122/1.549276

[20] Limbach H, Arnold A, Mann B and Holm C 2006 *Computer Physics Communications* **174** 704–727 ISSN 00104655 URL https://linkinghub.elsevier.com/retrieve/pii/S001046550500576X

[21] Krüger T, Kusumaatmaja H, Kuzmin A, Shardt O, Silva G and Viggen E M 2017 *The Lattice Boltzmann Method* Graduate Texts in Physics (Cham: Springer International Publishing) ISBN 978-3-319-44647-9 978-3-319-44649-3 URL http://link.springer.com/10.1007/978-3-319-44649-3

[22] Chai Z, Shi B, Guo Z and Rong F 2011 *Journal of Non-Newtonian Fluid Mechanics* **166** 332–342 ISSN 03770257 URL https://linkinghub.elsevier.com/retrieve/pii/S0377025711000073